

# Data-scarce surrogate modeling of shock-induced pore collapse process

S. W. Cheung, Y. Choi, H. K. Springer, T. Kadeethum

May 17, 2023

**Shock Waves** 

### Disclaimer

This document was prepared as an account of work sponsored by an agency of the United States government. Neither the United States government nor Lawrence Livermore National Security, LLC, nor any of their employees makes any warranty, expressed or implied, or assumes any legal liability or responsibility for the accuracy, completeness, or usefulness of any information, apparatus, product, or process disclosed, or represents that its use would not infringe privately owned rights. Reference herein to any specific commercial product, process, or service by trade name, trademark, manufacturer, or otherwise does not necessarily constitute or imply its endorsement, recommendation, or favoring by the United States government or Lawrence Livermore National Security, LLC. The views and opinions of authors expressed herein do not necessarily state or reflect those of the United States government or Lawrence Livermore National Security, LLC, and shall not be used for advertising or product endorsement purposes.

## Data-scarce surrogate modeling of shock-induced pore collapse process

Siu Wun Cheung<sup>1\*</sup>, Youngsoo Choi<sup>1</sup>, H. Keo Springer<sup>2</sup>, Teeratorn Kadeethum<sup>3</sup>

 <sup>1\*</sup>Center for Applied Scientific Computing, Lawrence Livermore National Laboratory, Livermore, 94550, CA, USA.
 <sup>2</sup>Material Science Division, Energetic Materials Center, Lawrence Livermore National Laboratory, Livermore, 94550, CA, USA.
 <sup>3</sup>Sandia National Laboratories, Albuquerque, 87185, NM, USA.

\*Corresponding author(s). E-mail(s): cheung26@llnl.gov; Contributing authors: choi15@llnl.gov; springer12@llnl.gov; tkadeet@sandia.gov;

#### Abstract

Understanding the mechanisms of shock-induced pore collapse is of great interest in various disciplines in sciences and engineering, including materials science, biological sciences, and geophysics. However, numerical modeling of the complex pore collapse processes can be costly. To this end, a strong need exists to develop surrogate models for generating economic predictions of pore collapse processes. In this work, we study the use of a data-driven reduced order model, namely dynamic mode decomposition, and a deep generative model, namely conditional generative adversarial networks, to resemble the numerical simulations of the pore collapse process at representative training shock pressures. Since the simulations are expensive, the training data are scarce, which makes training an accurate surrogate model challenging. To overcome the difficulties posed by the complex physics phenomena, we make several crucial treatments to the plain original form of the methods to increase the capability of approximating and predicting the dynamics. In particular, physics information is used as indicators or conditional inputs to guide the prediction. In realizing these methods, the training of each dynamic mode composition model takes only around 30 seconds on CPU. In contrast, training a generative adversarial network model takes 8 hours on GPU. Moreover, using dynamic mode decomposition, the final-time relative error is around 0.3% in the reproductive cases. We also demonstrate the predictive power of the methods at unseen testing shock pressures, where the error ranges from 1.3% to 5% in the interpolatory cases and 8% to 9% in extrapolatory cases.

Keywords: pore collapse, shock physics, reduced order modeling, machine learning

### 1 Introduction

Shock-induced pore collapse is a phenomenon that occurs when a shock wave passes through a porous material, causing the pores to collapse or deform. Figure 1 illustrates a shock-induced pore collapse process. At first, the shock approaches and travels through the pore. The pore eventually deforms and develops into a high-temperature profile after the interaction with the shock. This phenomenon has been observed and studied in a variety of materials, including viscoelastic materials [1], nanoporous metals [2], sedimentary rocks [3], biological cells [4], and polymers [5]. The collapse of pores can have a significant impact on the mechanical properties of the material, including its strength, stiffness, and ductility. For example, in metals, shock-induced pore collapse can lead to a reduction in ductility and toughness, which can make the material more prone to brittle failure. In geological materials, pore collapse can affect the permeability and porosity of the material, which can have implications for groundwater flow and oil recovery. Understanding the mechanisms of shock-induced pore collapse is therefore of great interest in various disciplines in sciences and engineering, including materials science, biological sciences and geophysics.

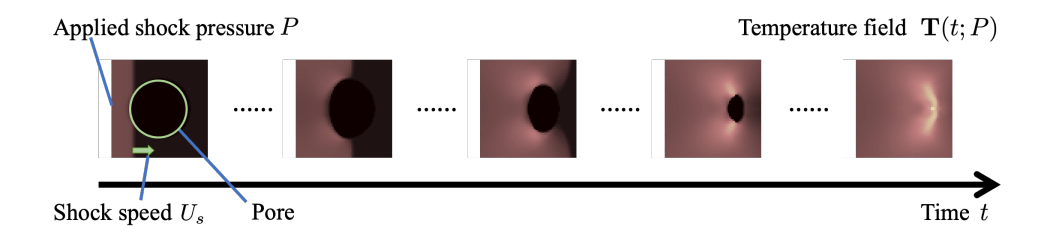


Fig. 1 Schematic diagram for illustration of shock-induced pore collapse process. At first, the shock approaches and travels through the pore. The pore eventually deforms and develops into a high-temperature profile after the interaction with the shock.

However, accurately analyzing the pore collapse dynamics is challenging due to the complex and nonlinear nature of the deformation process. Traditional analytical models, which rely on simplified assumptions about the material properties and pore geometry, often fail to capture the true behavior of the system. Numerical methods is a powerful alternative to obtain approximate solutions through computer simulation in this scenario. For instance, the pore collapse processes can be accurately simulated by the multi-physics hydro-code, ALE3D [6]. However, a single simulation takes up to

1 week on 1024 cores. It is therefore desirable to develop efficient techniques for resembling the dynamics in these computationally expensive simulations and predicting the dynamics in unseen generic shock pressures.

Obtaining computationally economical prediction of complex physics phenomena remains a demanding and challenging task in many applications in engineering and science. In recent years, numerous research efforts have been devoted to develop surrogate models, which work as simplified representation of the underlying physical process and reduce the computational cost of simulating or analyzing the original system. One important class of these surrogate models is the projection-based reduced order models (ROMs), which aims to reduce the dimensionality by projecting highfidelity physics-based models onto low-dimensional structures, which are constructed from compression of the representative snapshot solution data. The data compression techniques include linear approaches such as proper orthogonal decomposition (POD) [7], balanced truncation [8], and reduced basis method [9], or nonlinear compression approaches such as autoencoders (AE) [10–12]. Projection-based ROMs are intrusive in the sense that they involve incorporating the reduced solution representation into the governing equations, physics laws, and numerical discretization methods, such as finite element, finite volume, and finite difference methods. As a result, these approaches are data-driven but also constrained by physics, requiring less data to achieve the same level of accuracy. Surveys on the classical projection-based ROMs can be found in [13, 14]. Linear subspace ROMs had been applied to various applications which exhibit advection and transport phenomena, including Burgers equation and Euler equations in small-scale [15–17], Navier–Stokes equations [18, 19], Lagrangian hydrodynamics [20, 21], porous media flow [22, 23], shallow water equations [24, 25], Boltzmann transport problems [26], and wave equations [27–29].

Despite the successes of classical linear subspace projection-based ROMs in various applications, it is important to note that these approaches are limited to the cases where the intrinsic solution manifold can be represented by a low-dimensional subspace. This assumption is violated in problems with slow decay in the Kolmogorov n-width in the solution manifold, such as advection-dominated problems characterized by sharp gradients, moving shock fronts and turbulence, which hinders the practical use of linear subspace projection-based ROMs in related applications. To address this challenge, an alternative approach is to construct small yet accurate projection-based reduced-order models by decomposing the solution manifold into submanifolds. Local reduced-order models are constructed to approximate the solution within a specific subset of the parameter-time domain in the offline phase, are assigned based on the information of the parameter, time, and current system state in the online phase. The concept of a local reduced order model was introduced in [30, 31], where unsupervised clustering is used for the solution manifold decomposition. In [32, 33], windowed ROM approaches were introduced to construct temporally-local ROMs which are small but accurate within a short period in advection-dominated problems. In [20, 21], windowed ROM approaches were developed for Lagrangian hydrodynamics by decomposing the solution manifold decomposition based on physical time or more generally a suitably defined physics-based indicator.

A drawback of projection-based ROMs is that the implementation requires knowledge of the underlying numerical methods used in the high-fidelity simulation. Conversely, the class of non-intrusive surrogate models do not require access to the source code of the high-fidelity physics solver, and they are solely based on data. With the growing availability of data, there has been extensive research on non-intrusive surrogate models of discrete dynamics, using different dimensionality reduction and machine learning techniques. Similar to the projection-based ROMs, many nonintrusive surrogate models construct low-dimensional structure for approximating the solution manifold and approximate the dynamics in the low-dimensional latent code. While the projection-based ROMs use the governing equations to derive the dynamics in the low-dimensional latent space, non-intrusive surrogate models are purely data-driven. For example, several approaches use linear compression techniques, to construct a reduced subspace from snapshots, such as dynamic mode decomposition (DMD) [34–37] which seeks the best-fit linear model, operator inference (OpInf) [38– 40] which seeks the best-fit polynomial model, and sparse identification of nonlinear dynamics (SINDy) [41, 42] which seeks the best-fit sparse regression. With the recent advancements in representation learning by neural networks, the idea of identifying the best reduced discrete dynamic model within a certain family of functions can be extended to nonlinear compression techniques, for example, parametric Latent Space Dynamics Identification (LaSDI) [43, 44] and DeepFluids [45]. Besides dimensionality reduction techniques, neural networks can also be used to approximate the nonlinear operator in the dynamical system as non-intrusive surrogate models, such as Fourier neural operator (FNO) [46, 47], deep operator network (DeepONet) [48], and other relevant works [49–53], Moreover, recurrent neural network architecture can be used to model complex dynamical systems with memory effects [54].

In recent years, there has been growing research interests in dynamical modeling [55, 56] and surrogate modeling [57, 58] of the shock compression of a heterogeneous material with machine learning techniques. In this work, we employ and compare two data-driven and machine-learning based methods, namely dynamic mode decomposition (DMD) and U-Net generative adversarial networks, to serve as efficient non-intrusive surrogate models of the pore collapse dynamics. As illustrated in Figure 2, these methods are used to model the recurrent discrete dynamics and snapshot data from selected training shock pressure are used to train the model. Composition of the trained model is used to perform sequential prediction of the discrete dynamics of the pore collapse process at a general shock pressure. We remark that, since the simulations are expensive, the training data are scarce. To the best of our knowledge, this is the first work in using data-driven non-intrusive surrogate modeling methods for the pore collapse process. In our current work, we aim to focus on a restricted range of shock pressures to establish a foundational understanding of the limitations of existing ROM approaches in the pore collapse dynamics with pressuredependent rates. We make several crucial treatments to the plain original form of the methods in order to increase the capability of approximating and predicting the dynamics. For enhancing DMD, we combine the idea of physics-indicated local ROM in [20, 21] and parametric DMD with matrix manifold interpolation in [59–61]. On

the other hand, for enhancing GAN, we combine the improved architecture with conditional continuous input in [62] and the residual network structure for approximating discrete dynamics (c.f. [53]).

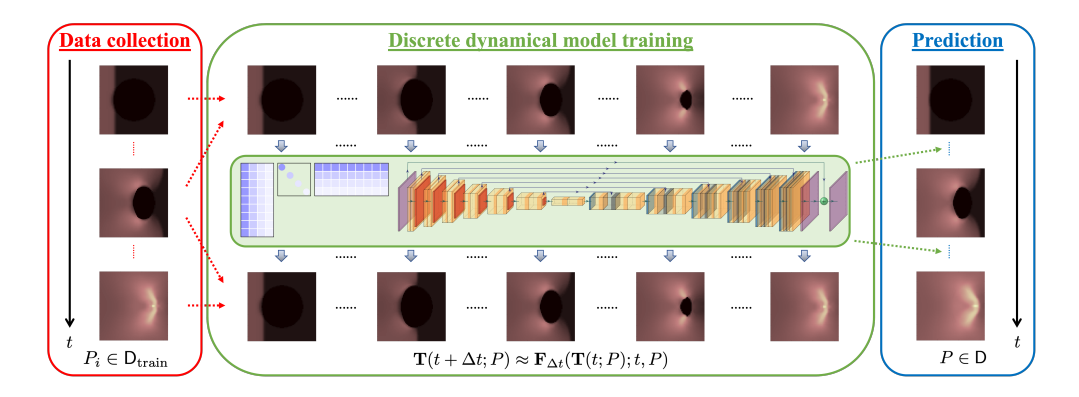


Fig. 2 Schematics of non-intrusive surrogate models of the discrete dynamics of pore collapse. In the offline phase, the snapshot data from training shock pressures are used as the input and the output of the recurrence relation in the discrete dynamics, and dynamic mode decomposition or U-Net generative adversarial networks are employed as functional approximation to model the relation. In the online phase, composition of the trained model is used to perform sequential prediction of the discrete dynamics of pore collapse process at a general shock pressure.

The rest of the paper is organized as follows. In Section 2, we present the details of the material model. In Section 3, we describe the phenomenon of pore collapse process and the physics-based high-fidelity simulations. Next, in Section 4 and Section 5, we discuss the details of surrogate modeling by DMD and GAN, respectively. In Section 6, we present some numerical results to test and compare the performance of the proposed methods. Finally, a conclusion is given in Section 7.

### 2 Energetic Material Model

In this section, we discuss the constitutive models employed for the energetic material properties, including the shear modulus, strength, melt curve, melt viscosity, unreacted equation of state (EOS), and heat capacity. A similar material model is developed in [58] with the exception that the strength model has been simplified in this work to minimize shear localization effects for ease of training surrogate model.

### 2.1 Shear Modulus

MD predictions [63] for the Voigt-Reuss-Hill average shear modulus ( $G_{VRH}$ ) are fit to the Steinberg-Guinan pressure- and temperature-dependent shear modulus model [64] given by,

 $G(P,T) = G_0 \left[ 1 + a_P P \eta^{-1/3} - a_T (T - 300) \right]$  (1)

where  $G_0$  is the shear modulus at ambient conditions,  $\eta$  is the compression,  $a_P$  is the pressure dependence coefficient, and  $a_T$  is the temperature dependence coefficient.

This model better accounts for elastic stiffening under shock conditions compared to our previous use of a constant shear modulus. Model parameter values are shown in Table 1. Shear modulus model calibration is completed prior to strength model calibration since it is used in the latter.

 Table 1
 Steinberg-Guinan

 shear modulus parameters

Parameter	Value
$G_0$ (GPa)	7.37
$a_P \text{ (GPa}^{-1})$	1848
$a_T  ({\rm K}^{-1})$	$3.67 \times 10^{-4}$

### 2.2 Strength

For the strength, we use the Johnson-Cook model [65] with a von Mises yield criterion. It is an isotropic model with strain, strain-rate, and temperature dependencies that is given by,

$$Y = \left(\frac{G(P,T)}{G_0}\right) \left[ (A + B\bar{\epsilon}_{\mathbf{p}}^n) \left( 1 + C \ln \left( \frac{\dot{\bar{\epsilon}_{\mathbf{p}}}}{\dot{\epsilon}_0} \right) \right) \left( 1 - \left( \frac{T - T_{\text{room}}}{T_{\text{m}} - T_{\text{room}}} \right)^m \right) \right]$$
(2)

where  $\frac{G(P,T)}{G_0}$  is the shear modulus factor, A and B are initial yield strength and strain-hardening parameters, n is the strain-hardening coefficient, C is the strain-rate coefficient,  $\dot{\epsilon}_0$  is the reference strain rate,  $\dot{\bar{\epsilon}}_p$  is the equivalent plastic strain rate, m is the temperature dependence exponent,  $T_{\text{room}}$  is the room temperature, and  $T_{\text{m}}$  is the melt temperature. The use of  $\frac{G(P,T)}{G_0}$  additionally accounts for the effects of pressure-and temperature-dependent elasticity on strength.

The model is calibrated to strength measurements on high solid loading energetic formulations and single crystal data. This includes split Hopkinson pressure bar data in the  $\sim 10^3~\rm s^{-1}$  strain rate regime [66] and weak shock data in the  $\sim 10^6~\rm s^{-1}$  strain rate regime [67, 68]. Johnson-Cook strength model parameters are shown in Table 2. Parameter set differences with previous Johnson-Cook models [69] are primarily due to the addition of  $\frac{G(P,T)}{G_0}$ . Reduced model fitting error is realized using a reference rate of 2000  $\rm s^{-1}$  which is the rate of the split Hopkinson pressure bar measurements.

### 2.3 Melt Curve

Pressure-dependent melt curves are used in conjunction with the Johnson-Cook model to describe the degradation of strength as the material approaches the melting temperature. Accurate melt curves are important for predicting the plastic work and heating which influences the hot spots. A Simon-Glatzel form [70] is fit to MD predictions of

**Table 2** Johnson-Cook strength model parameters

Parameter	Value
A (MPa)	46.8
B  (MPa)	46.8
n	0.1
C	1.8
$\dot{\epsilon}_0 \; ({\rm s}^{-1})$	2250
m	3
$T_{\text{room}}$	300

Kroonblawd & Austin [71]. It is given by,

$$T_{\rm m} = T_{\rm m,ref} \left[ 1 + \left( \frac{P - P_{\rm ref}}{a} \right)^{\frac{1}{c}} \right]$$
 (3)

where  $T_{\rm m,ref}$  is the melting point at the reference pressure  $(P_{\rm ref})$  and a and c are fitting parameters. Model parameters are shown in Table 3.

Table 3 Simon-Glatzel melt curve parameters based on MD predictions of Kroonblawd & Austin [71]

Parameter	Value
$T_{\rm m,ref}$ (K)	551
$P_{\rm ref}$ (GPa)	0
a (GPa)	0.305
c	3.270

### 2.4 Melt Viscosity

A pressure- and temperature-dependent melt viscosity model informed by MD simulations [71] replaces a constant viscosity used in the previous studies [69]. This change improves viscous heating predictions in molten shear bands. The model is given by,

$$\eta(T, P) = \eta^0 \left( 1 + \frac{P}{P^0} \right)^{n_p} \exp\left[ \frac{T_a(P)}{T} \right]$$

$$T_a(P) = T^* \sum_{n=0}^M a_n \left( \frac{P}{P^0} \right)^n$$
(4)

Fitting parameters are shown in Table 4.

**Table 4** Shear viscosity model parameters [71]

Parameter	Value
$\eta^0 \text{ (mPa-s)}$	$4.605 \times 10^{-4}$
$P^0$ (GPa)	$1.190 \times 10^{-1}$
$T^*$ (K)	293
$n_{ m p}$	1.330
$\dot{M}$	2
$a_0$	$2.551\times10^{1}$
$a_1$	$1.473 \times 10^{-1}$
$a_2$	$7.683 \times 10^{-4}$

### 2.5 Unreacted EOS

We use a modified form of the Murnaghan EOS for the unreacted energetic material [72],

$$P = \frac{K}{n} \left[ \left( \frac{1}{v} \right)^n - \exp\left( -n\alpha (T - T_0) \right) \right]$$
 (5)

where K is the bulk modulus, n is the derivative  $\mathrm{d}K/\mathrm{d}P$ , v is the relative volume,  $\alpha$  is the volumetric coefficient of thermal expansion, and  $T_0$  is the reference temperature. When  $T=T_0$  for the isothermal case, the exponential term is unity and this model reverts to the temperature independent form,  $K/n\left[(1/v)^n-1\right]$ . Parameters were simultaneously fit to Hugoniot [73] and isothermal data [74–76] for the temperature dependent and temperature independent forms of the model, respectively. The bulk modulus is set to 21 GPa [76] which sufficiently fit a range of low and high pressure data. Model parameters are shown in Table 5.

**Table 5** Murnaghan EOS parameters

Parameter	Value
$\rho_0$ (g/cc)	1.90
n	4.48
K (GPa)	21.0 [66]
$\alpha (K^{-1})$	$1.31 \times 10^{-4}$ [77]
$T_0$ (K)	298

### 2.6 Heat Capacity

We use an Einstein oscillator heat capacity model to obtain accurate temperatures for the unreacted explosive which is given by,

$$\frac{C_p(T)}{R} = \sum_{i=1}^{N} A_i \frac{\left(\frac{\Theta_i}{T}\right)^2 \exp\left(\frac{\Theta_i}{T}\right)}{\left(\exp\left(\frac{\Theta_i}{T}\right) - 1\right)^2} \tag{6}$$

where oscillators are specified in pairs  $(A_i, \Theta_i)$ . We fit the model to lower temperature heat capacity measurements [78] shown in Table 6 and the Dulong-Petit high

temperature limit at 3000 K. The limit is typically calculated as  $3N_{\rm A}R/M_{\rm HMX}$  where  $N_{\rm A}$  is the number of atoms (= 28), R is the universal gas constant, and  $M_{\rm HMX}$  is the molecular weight of HMX (= 296.155 g/mol). However, based on [77], we subtract eight degrees-of-freedom based on eight C-H bonds stretching because those are very high vibrational frequencies and not highly populated, i.e., don't contribute significantly to storing heat. This modifies the equation to  $3(N_{\rm A}-8)R/M_{\rm HMX}$  which gives 2.12 J/g-K. This limit is taken at a temperature of 3000 K [77]. Model parameters are shown in Table 7.

Table 6 HMX heat capacity measurements [78].

T (K)	$C_p \text{ (J/g-K)}$
310	1.052
375	1.201
440	1.351

Parameter	Value
$A_1$	$4.822 \times 10^{1}$
$\Theta_1$ (K)	$1.528 \times 10^{3}$
$A_2$	$2.881 \times 10^{1}$
$\Theta_2$ (K)	-3.750

### 3 ALE3D simulations of pore collapse

In this section, we describe the pore collapse problem and the details of the ALE3D simulations. The domain consists of an impact region and an energetic grain region of interest used for surrogate modeling training. The size of the energetic grain is 10  $\mu m$  by 10  $\mu m$  with a central circular pore whose diameter is 1  $\mu m$ . Prescribed initial velocities are assigned to the impact region, under 2D plane strain conditions and symmetry conditions on the upper and lower boundaries of the domain. A range of 11 to 15 GPa of shock loading pressures is applied. The pore collapse simulation is performed with the multi-physics arbitrary Lagrangian Eulerian finite element hydrocode, ALE3D [6], coupled with LLNL's thermochemical code Cheetah to handle the equation of states. The numerical zone size and time step size used in this study are 25 nm and 2.5 ns respectively, and the computational domain is decomposed into 537200 zones. Figure 3 depicts some selected representative snapshots of temperature fields of resolution  $128 \times 128$  in a subsampled spatial region of interest, which is a square with side length 1.6  $\mu$ m around the pore and comprised of 16384 zones, at different shock pressures ranging from 11 to 15 GPa, and time instances ranging from 0.8 to 1.4  $\mu$ s. Each row corresponds to the same shock pressure and each column corresponds to same

time instance. It can be observed that, with higher shock pressure, the pore collapse takes place at an earlier time and a faster rate, and the resultant peak temperature is higher.

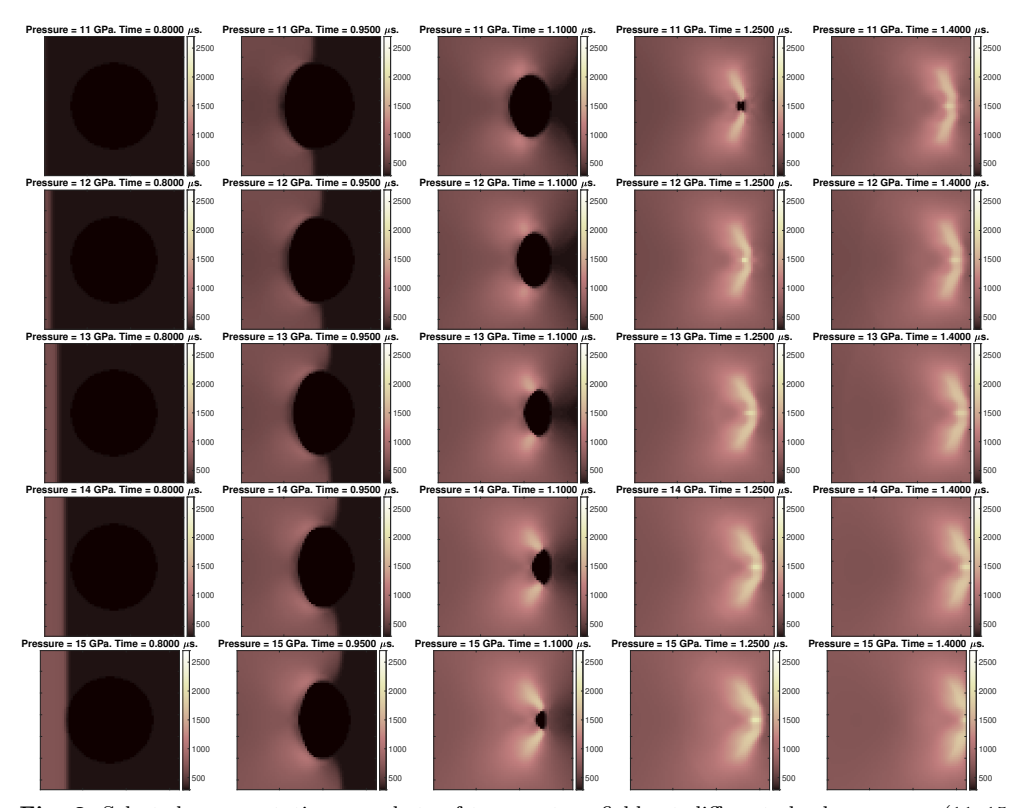


Fig. 3 Selected representative snapshots of temperature fields at different shock pressures (11–15 GPa, row-wise) and time instances (0.8–1.4  $\mu$ s, column-wise). With higher shock pressure, the pore collapse takes place at an earlier time.

Next, we introduce some notations and dimensionless quantities to simplify the discussion. Let  $\mathsf{D} = [P_{\min}, P_{\max}]$  denote the range of applied shock pressure measured in GPa,  $[0,T_{\mathrm{f}}]$  be the temporal domain measured in ns, and  $\Omega \subset \mathbb{R}^2$  be the spatial computational domain with length scale in nm. In the numerical simulations, the discrete temperature fields are defined in square sub-zones with equal length  $h_x$  in  $\Omega$ , at a uniform time increment  $\Delta t$ . To focus on the pore collapse dynamics, the domains are subsampled. The spatial region of interest  $\Omega_{\mathrm{obs}} = [x_{\min}, x_{\max}]^2 \subset \Omega$  is chosen around the pore, and the time interval of interest is denoted by  $\mathcal{T}(P) = [t^{(0)}(P), t^{(0)}(P) + m\Delta t] \subset [0, T_{\mathrm{f}}]$  for a shock pressure  $P \in \mathbb{D}$ . It is important to note that, since the dynamics is advective and transport in nature and the traveling speed of the shock varies with shock pressure, in order to capture the corresponding physics phenonemena, the initial time  $t^{(0)}(P)$  must be adjusted depending on the shock pressure P.

We end this section by describing the data sampling for constructing reduced order models. We denote the resolution of the spatial region of interest  $\Omega_{\rm obs}$  by  $N_x = (x_{\rm max} - x_{\rm min})/h_x$ . The discrete temperature fields are represented as matrices  $T(t;P) \in \mathbb{R}^{N_x \times N_x}$  or vectors  $T(t;P) \in \mathbb{R}^{N_x^2}$ , depending on the surrogate modeling approach under consideration. The samples of temperature fields  $T_i^k = T(t_i^{(k)}; P_i)$  are measured at training shock pressures  $\mathsf{D}_{\text{train}} = \{P_i\}_{i=1}^{N_P} \subset \mathsf{D}$  and time instances  $t_i^{(k)} = t^{(0)}(P_i) + k\Delta t$  for  $0 \le k \le m$  within the time interval  $\mathcal{T}_i = \mathcal{T}(P_i)$ . Our goal is to construct reduced order models from the training samples to resemble the numerical simulations of pore collapse process, and make predictions of the temperature fields T(t;P) in the time interval of query  $t \in \mathcal{T}(P)$ , given the initial condition  $T^{(0)}(P) = T(t^{(0)}(P);P)$ , at generic shock pressures  $P \in \mathsf{D} \setminus \mathsf{D}_{\rm train}$ . In the rest of this paper, we will introduce techniques to overcome the difficulties posed to surrogate modeling by the advective and transport nature of the dynamics.

### 4 Dynamic mode decomposition

Dynamic mode decomposition (DMD) was introduced in [34] as a numerical technique for extracting discrete dynamical features from a sequence of sample data and further studied in [35, 36]. We will given a brief overview of DMD in Section 4.1 in the context of numerical simulation data. Next, in Section 4.2, we will discuss a specific approach of modifying DMD to tackle the challenges from the nature of advective and transport of the shock front. In Section 4.3, we will introduce the predictive procedure of DMD on generic shock pressure  $P \in D$ , which is in general unseen in the training samples.

### 4.1 Offline stage: serial DMD

We start the offline procedure in DMD with the sequence of samples  $\{\boldsymbol{T}_i^{(k)}\}_{k=0}^m$  at a particular training shock pressure  $P_i \in \mathsf{D}_{\mathsf{train}}$ . The samples  $\{\boldsymbol{T}_i^{(k)}\}_{k=0}^m$  are represented as vectors in  $\mathbb{R}^{N_x^2}$ . DMD seeks a linear transformation  $\mathbf{A}_i \in \mathbb{R}^{N_x^2 \times N_x^2}$  which approximates the discrete dynamics

$$T_i^{(k+1)} \approx \mathbf{A}_i T_i^{(k)} \text{ for all } 0 \le k < m.$$
 (7)

The input snapshot matrix  $\mathbf{S}_i^-$  and the output snapshot matrix  $\mathbf{S}_i^+$  of the linear recurrence relation are

$$\mathbf{S}_{i}^{-} = \left[ \boldsymbol{T}_{i}^{(0)}, \boldsymbol{T}_{i}^{(1)}, \cdots, \boldsymbol{T}_{i}^{(m-1)} \right] \in \mathbb{R}^{N_{x}^{2} \times m},$$

$$\mathbf{S}_{i}^{+} = \left[ \boldsymbol{T}_{i}^{(1)}, \boldsymbol{T}_{i}^{(2)}, \cdots, \boldsymbol{T}_{i}^{(m)} \right] \in \mathbb{R}^{N_{x}^{2} \times m}.$$
(8)

Performing rank-r truncated singular value decomposition (SVD) on  $\mathbf{S}_{i}^{-}$  yields

$$\mathbf{S}_{i}^{-} = \mathbf{U}_{i} \mathbf{\Sigma}_{i} \mathbf{V}_{i}^{\top}, \tag{9}$$

where  $\mathbf{U}_i \in \mathbb{R}^{N_x^2 \times r}, \mathbf{\Sigma}_i \in \mathbb{R}^{r \times r}, \mathbf{V}_i \in \mathbb{R}^{m \times r}$ , and  $r \leq \operatorname{rank}(\mathbf{S}^-) \leq \min\{m, N_x^2\}$ . We remark that the reduced dimension r is assumed to be identical for all training parameters in  $\mathbf{D}_{\text{train}}$ . Then we define the reduced discrete dynamical system by

$$\widehat{\mathbf{A}}_i = \mathbf{U}_i^{\mathsf{T}} \mathbf{S}_i^+ \mathbf{V}_i \mathbf{\Sigma}_i^{-1} \in \mathbb{R}^{r \times r}, \tag{10}$$

and perform the spectral decomposition on  $\hat{\mathbf{A}}_i$ , i.e.,

$$\widehat{\mathbf{A}}_i \mathbf{X}_i = \mathbf{X}_i \mathbf{\Lambda}_i, \tag{11}$$

where  $\mathbf{X}_i \in \mathbb{C}^{r \times r}$  consists of the eigenvectors of  $\widehat{\mathbf{A}}_i$  and  $\mathbf{\Lambda}_i \in \mathbb{C}^{r \times r}$  is the diagonal matrix containing the DMD eigenvalues. The DMD basis is then given by  $\mathbf{\Phi}_i = \mathbf{U}_i \mathbf{X}_i \in \mathbb{C}^{N_x^2 \times r}$ . Then the DMD modes  $(\mathbf{\Phi}_i, \mathbf{\Lambda}_i)$  are used for reproductive approximation  $\widetilde{T}_{\text{DMD}}(t; P_i)$  of the dynamics at the shock pressure  $P_i$ , which is given by: for  $t \in \mathcal{T}_i = [t_i^{(0)}, t_i^{(m)}]$ ,

$$\widetilde{\boldsymbol{T}}_{\mathrm{DMD}}(t; P_i) = \boldsymbol{\Phi}_i \boldsymbol{\Lambda}_i^{\frac{t - t_i^{(0)}}{\Delta t}} \boldsymbol{\Phi}_i^{\dagger} \boldsymbol{T}_i^{(0)}. \tag{12}$$

### 4.2 Offline stage: windowed DMD

Section 4.1 presented a serial DMD, in which the high-fidelity temperature fields are represented by ROM subspaces. However, the advective-dominated nature of the temperature field implies the weak linear dependence among the snapshots. As a result, there is no intrinsic low-dimensional subspace that can universally approximate the solution manifold comprised of all the solutions over the temporal domain. In mathematical terms, the manifold of temperature field in a single shock pressure has slow decay in the Kolmogorov n-width. As a result, maintaining accuracy over longer simulation times requires large-dimensional reduced subspaces. Moreover, the storage and computational burden associated with a large number of high-fidelity snapshot samples can be significant for SVD computations.

To address this challenge, we construct small yet accurate local projection-based reduced-order models to approximate the solution within a specific subset of the parameter-time domain in the offline phase, assign these ROMs based on the information of the parameter, time, and current system state in the online phase. The concept of localization has been well studied in the literature [20, 21, 32, 33]. The rationale is to decompose the solution manifold into submanifolds where the Kolmogorov n-width decays fast with respect to the subspace dimension, within which we can collect snapshots with strong linear dependence, which enables us to build accurate multiple low-dimensional approximating subspaces. The key ingredient of localization is a suitable indicator for clustering and classification. During the offline phase, each reduced-order model is constructed from a small subset of snapshot samples to ensure a low-dimensional representation. In the online phase, these reduced-order models are utilized within specific subsets of the parameter-time domain where they can provide accurate approximations.

Following [21], the windowed DMD framework employed in this paper entails a decomposition of the solution manifold by a displacement-based indicator which are efficient in clustering solution manifold describing transport dynamics. We describe the general framework of indicator-based decomposition of the solution manifold from which we will derive two practical examples later in this section. Let  $\Psi: \mathbb{R}^{N_x^2} \times \mathbb{R}^+ \times D \to \mathbb{R}$  be an indicator which maps the triplet (T, t, P) to a real value in the range  $[\Psi_{\min}, \Psi_{\max}]$ . For any  $P \in D$ , we assume  $\Psi(T^{(0)}(P), t^{(0)}(P), P) = \Psi_{\min}$ , and  $\Psi(T(t, P), t, P)$  is increasing with time t. The range of the indicator is partitioned into J subintervals, i.e.,

$$\Psi_{\min} = \Psi_0 < \Psi_1 < \dots < \Psi_{J-1} < \Psi_J = \Psi_{\max}. \tag{13}$$

In the training phase, at a given training parameter  $P_i \in D$ , instead of directly assembling all the snapshot samples into huge snapshot matrices as in (8), the FOM states are first classified into J groups. Given the samples  $\{T_i^{(k)}\}_{k=0}^m$  at a shock pressure  $P_i \in D_{\text{train}}$  and a group index  $1 \leq j \leq J$ , we denote by  $\mathcal{G}_i^{(j)}$  the subset of temporal indices whose corresponding snapshot belongs to the j-th group, i.e.,

$$\mathcal{G}_{i}^{(j)} = \left\{ 0 \le k < m : \Psi\left(\mathbf{T}_{i}^{(k)}, t_{i}^{(k)}, P_{i}\right) \in [\Psi_{j-1}, \Psi_{j}) \right\}, \tag{14}$$

and denote  $K_i^{(j-1)} = \min \mathcal{G}_i^{(j)}$  and  $m_i^{(j)} = |\mathcal{G}_i^{(j)}|$ . Then  $m = \sum_{j=1}^J m^{(j)}$ . Consequently, by extending  $K_i^{(J)} = m$  and taking  $\tau_i^{(j)} = t_{K_i^{(j)}}$  for  $0 \le j \le J$ , the time interval  $\mathcal{T}_i = [t_i^{(0)}, t_i^{(m)}]$  at the shock pressure  $P_i$  is partitioned into J subintervals, i.e.,

$$t_i^{(0)} = \tau_i^{(0)} < \tau_i^{(1)} < \dots < \tau_i^{(J-1)} < \tau_i^{(J)} = t_i^{(m)}. \tag{15}$$

For  $1 \le i < N_P$  and  $1 \le j \le J$ , we define the snapshot submatrices by

$$\mathbf{S}_{i}^{(j),-} = \left[\boldsymbol{T}_{i}^{(k)}\right]_{k \in \mathcal{G}_{i}^{(j)}} \in \mathbb{R}^{N_{x}^{2} \times m_{i}^{(j)}},$$

$$\mathbf{S}_{i}^{(j),+} = \left[\boldsymbol{T}_{i}^{(k+1)}\right]_{k \in \mathcal{G}_{i}^{(j)}} \in \mathbb{R}^{N_{x}^{2} \times m_{i}^{(j)}}.$$

$$(16)$$

By carrying out the truncated SVD as discussed in Section 4.1 with the pair of snapshot matrices  $(\mathbf{S}_i^{(j),-},\mathbf{S}_i^{(j),+})$ , we obtain the modal discrete dynamical system  $(\mathbf{U}_i^{(j)},\widehat{\mathbf{A}}_i^{(j)}) \in \mathbb{R}^{N_x^2 \times r_j} \times \mathbb{R}^{r_j \times r_j}$  by

$$\mathbf{S}_{i}^{(j),-} = \mathbf{U}_{i}^{(j)} \boldsymbol{\Sigma}_{i}^{(j)} \left[ \mathbf{V}_{i}^{(j)} \right]^{\top},$$

$$\widehat{\mathbf{A}}_{i}^{(j)} = \left[ \mathbf{U}_{i}^{(j)} \right]^{\top} \mathbf{S}_{i}^{(j),+} \mathbf{V}_{i}^{(j)} \left[ \boldsymbol{\Sigma}_{i}^{(j)} \right]^{-1}.$$
(17)

Again, it is assumed that the reduced dimension  $r_j$  is identical for all training parameters in  $D_{\rm train}$ . Then we perform eigenvalue decomposition as in Section 4.1 and obtain

the DMD modes  $(\mathbf{\Phi}_i^{(j)}, \mathbf{\Lambda}_i^{(j)}) \in \mathbb{C}^{N_x^2 \times r_j} \times \mathbb{C}^{r_j \times r_j}$  by

$$\widehat{\mathbf{A}}_{i}^{(j)} \mathbf{X}_{i}^{(j)} = \mathbf{X}_{i}^{(j)} \mathbf{\Lambda}_{i}^{(j)},$$

$$\mathbf{\Phi}_{i}^{(j)} = \mathbf{U}_{i}^{(j)} \mathbf{X}_{i}^{(j)},$$
(18)

which are used for the DMD reproductive approximation  $\widetilde{T}_{\text{DMD}}(t; P_i)$  at the shock pressure  $P_i$  given by: iteratively for  $1 \leq j \leq J$ , for  $t \in [\tau_i^{(j-1)}, \tau_i^{(j)}]$ ,

$$\widetilde{\boldsymbol{T}}_{\mathrm{DMD}}(t; P_i) = \boldsymbol{\Phi}_i^{(j)} \left[ \boldsymbol{\Lambda}_i^{(j)} \right]^{\frac{t - \tau_i^{(j-1)}}{\Delta t}} \left[ \boldsymbol{\Phi}_i^{(j)} \right]^{\dagger} \widetilde{\boldsymbol{T}}_{\mathrm{DMD}}(\tau_i^{(j-1)}; P_i), \tag{19}$$

where  $\widetilde{T}_{\rm DMD}(\tau_i^{(j-1)}; P_i)$  is set to be the initial state  $T_i^{(0)}$  if j=1, and is obtained from DMD approximation in the previous time subinterval for j>1. We remark that if J=1, it reduces to the serial DMD as discussed in Section 4.1.

We end this subsection with two practical choices of the indicator  $\Psi$  for the decomposition of solution manifold. One natural choice is the time windowing (TW) DMD, where we use the physical time as the indicator, i.e.,  $\Psi(T,t,P)=(t-t^{(0)}(P))/\Delta t$ . In this case,  $\Psi_{\min}=0$  and  $\Psi_{\max}=m$ , and the temporal partition (15) is actually an affine transformation of indicator range partition (13), i.e.  $\tau_i^{(j)}=t_i^{(0)}+\Psi_j\Delta t$ , for all  $1\leq j\leq J$ .

Inspired by [21], another choice of indicator-based decomposition of solution manifold that is applicable to pore collapse process is the distance windowing (DW) DMD, where we use the horizontal translation distance of the primary shock as the indicator. Among the  $N_x^2$  sub-zones, we select  $N_x$  sub-zones on the bottom boundary  $x_2 = x_{\min}$  as markers, and collect their indices into a subset  $\mathcal{I}$ . Then the indicator of shock distance is defined as the number of markers whose temperature values exceed the temperature threshold  $T_{\text{threshold}}$ , which is the critical value distinguishing between the dark background temperature and the bright hot temperature as illustrated in Figure 1, i.e.,

 $\Psi(\boldsymbol{T},t,P) = \left| \left\{ s \in \mathcal{I} : \mathbf{e}_s^\top \boldsymbol{T} > T_{\text{threshold}} \right\} \right|.$  In this case,  $\Psi_{\min} \geq 0$  and  $\Psi_{\max} = N_x$ .

### 4.3 Prediction stage

For parametric DMD prediction at a generic shock pressure  $P \in \mathbb{D}$ , we construct an appropriate temporal partition and use corresponding DMD models for approximation in each of temporal subintervals. More precisely, for  $1 \leq j \leq J$ , we need to determine the temporal subinterval endpoint  $\tau^{(j)}(P) \in \mathbb{R}$  by scalar-valued interpolation, and the modal discrete dynamical system  $(\mathbf{U}^{(j)}(P), \widehat{\mathbf{A}}^{(j)}(P)) \in \mathbb{R}^{N_x^2 \times r_j} \times \mathbb{R}^{r_j \times r_j}$  by matrix-valued interpolation, with the interpolating points as the training shock pressures in  $\mathbf{D}_{\text{train}}$  and the interpolating values in the database obtained at the training shock pressures as described in Section 4.2, i.e.,

$$\mathcal{DB}^{(j)} = \left\{ \left( P_i, \tau_i^{(j)}, \mathbf{U}_i^{(j)}, \widehat{\mathbf{A}}_i^{(j)} \right) \right\}_{i=1}^{N_P} \subset \mathsf{D}_{\mathrm{train}} \times \mathbb{R} \times \mathbb{R}^{N_x^2 \times r_j} \times \mathbb{R}^{r_j \times r_j}. \tag{20}$$

We adopt the radial basis functions (RBF) interpolation method. We choose an infinitely smooth radial basis function  $\varphi : [0, \infty) \to [0, \infty)$ , and define the interpolation matrix  $\mathbf{B} \in \mathbb{R}^{N_P \times N_P}$  by

$$\mathbf{B}_{i,i'} = \varphi(\|P_i - P_{i'}\|) \text{ for all } 1 \le i, i' \le N_P.$$

The scalar-valued interpolant of the temporal subinterval endpoint  $\tau^{(j)}(P) \in \mathbb{R}$  is given by the linear combination

$$\tau^{(j)}(P) = \sum_{i=1}^{N_P} \omega_i^{(j)} \varphi(\|P - P_i\|), \qquad (21)$$

where the weights  $\boldsymbol{\omega}^{(j)} = (\omega_1^{(j)}, \omega_2^{(j)}, \dots, \omega_{N_P}^{(j)})^{\top} \in \mathbb{R}^{N_P}$  are defined by solving  $\mathbf{B}\boldsymbol{\omega}^{(j)} = \boldsymbol{\tau}^{(j)} = (\tau_1^{(j)}, \tau_2^{(j)}, \dots, \tau_{N_P}^{(j)})^{\top} \in \mathbb{R}^{N_P}$ , which is derived from

$$\tau^{(j)}(P_i) = \tau_i^{(j)} \text{ for all } 1 \le i \le N_P.$$

The interpolated values form a partition for the time interval of query  $\widetilde{\mathcal{T}}(P) = [\tau^{(0)}(P), \tau^{(J)}(P)] \subset \mathcal{T}(P)$ , i.e.,

$$\tau^{(0)}(P) < \tau^{(1)}(P) < \dots < \tau^{(J-1)}(P) < \tau^{(J)}(P). \tag{23}$$

It remains to describe the matrix-valued interpolation. For a comprehensive discussion on the theory and practice of interpolation on a matrix manifold in the context of linear subspace reduced order models, the reader is referred to [59–61]. Here, we present only the necessary details of RBF interpolation of DMD matrix components at a generic shock pressure  $P \in D$ . The first step is identify a reference training shock pressure index  $1 \le i_{\rm ref}(P) \le N_P$  by

$$i_{\text{ref}}(P) = \underset{1 < i < N_P}{\arg \min} |P - P_i|. \tag{24}$$

Next, we rotate the reduced order operator to enforce the consistency in the generalized coordinate system. For  $1 \leq i \leq N_P$ , we perform SVD of the matrix product  $\left[\mathbf{U}_i^{(j)}\right]^{\top}\mathbf{U}_{i_{\text{ref}}(P)}^{(j)}$ , i.e.,

$$\left[\mathbf{U}_{i}^{(j)}\right]^{\top}\mathbf{U}_{i_{\text{ref}}(P)}^{(j)} = \left[\mathbf{Y}_{i}^{(j)}(P)\right]^{\top}\boldsymbol{\Gamma}_{i}^{(j)}(P)\mathbf{Z}_{i}^{(j)}(P). \tag{25}$$

Then we define the rotation matrix  $\mathbf{Q}_i^{(j)}(P) \in \mathbb{R}^{r_j \times r_j}$  by

$$\mathbf{Q}_{i}^{(j)}(P) = \left[\mathbf{Y}_{i}^{(j)}(P)\right]^{\mathsf{T}} \mathbf{Z}_{i}^{(j)}(P), \tag{26}$$

which is the solution to the classical orthogonal Procrustes problem. The matrix-valued interpolant of the modal discrete dynamical system  $(\mathbf{U}^{(j)}(P), \widehat{\mathbf{A}}^{(j)}(P)) \in \mathbb{R}^{N_x^2 \times r_j} \times \mathbb{R}^{r_j \times r_j}$  is then given by the linear combination

$$\mathbf{U}^{(j)}(P) = \mathbf{U}_{i_{\text{ref}}(P)}^{(j)} + \sum_{i=1}^{N_P} \mathbf{F}_{i}^{(j)}(P)\varphi(\|P - P_i\|),$$

$$\widehat{\mathbf{A}}^{(j)}(P) = \widehat{\mathbf{A}}_{i_{\text{ref}}(P)}^{(j)} + \sum_{i=1}^{N_P} \mathbf{G}_{i}^{(j)}(P)\varphi(\|P - P_i\|).$$
(27)

Here, for  $1 \leq \ell_1 \leq N_x^2$  and  $1 \leq \ell_2 \leq r_j$ , the  $(\ell_1, \ell_2)$ -entry of the weights  $\mathbf{F}_i^{(j)}(P) \in \mathbb{R}^{N_x^2 \times r_j}$ , denoted by  $\mathbf{f}_{\ell_1, \ell_2}^{(j)}(P) = \left( [\mathbf{F}_i^{(j)}(P)]_{\ell_1, \ell_2} \right)_{i=1}^{N_P} \in \mathbb{R}^{N_P}$ , are defined by solving

$$\mathbf{Bf}_{\ell_1,\ell_2}^{(j)}(P) = \left( \left[ \mathbf{U}_i^{(j)} \mathbf{Q}_i^{(j)}(P) - \mathbf{U}_{i_{\text{ref}}(P)}^{(j)} \right]_{\ell_1,\ell_2} \right)_{i=1}^{N_P} \in \mathbb{R}^{N_P}.$$
 (28)

Similarly, for  $1 \leq \ell_1, \ell_2 \leq r_j$ , the  $(\ell_1, \ell_2)$ -entry of the weights  $\mathbf{G}_i^{(j)}(P) \in \mathbb{R}^{r_j \times r_j}$ , denoted by  $\mathbf{g}_{\ell_1, \ell_2}^{(j)}(P) = \left( [\mathbf{G}_i^{(j)}(P)]_{\ell_1, \ell_2} \right)_{i=1}^{N_P} \in \mathbb{R}^{N_P}$ , are defined by solving

$$\mathbf{Bg}_{\ell_{1},\ell_{2}}^{(j)}(P) = \left( \left[ \mathbf{Q}_{i}^{(j)}(P)^{\top} \widehat{\mathbf{A}}_{i}^{(j)} \mathbf{Q}_{i}^{(j)}(P) - \widehat{\mathbf{A}}_{i_{\text{ref}}(P)}^{(j)} \right]_{\ell_{1},\ell_{2}} \right)_{i=1}^{N_{P}} \in \mathbb{R}^{N_{P}}.$$
(29)

As in Section 4.1, we perform eigenvalue decomposition and obtain the DMD modes  $(\Phi^{(j)}(P), \Lambda^{(j)}(P) \in \mathbb{C}^{N_x^2 \times r_j} \times \mathbb{C}^{r_j \times r_j})$  by

$$\widehat{\mathbf{A}}^{(j)}(P)\mathbf{X}^{(j)}(P) = \mathbf{X}^{(j)}(P)\mathbf{\Lambda}^{(j)}(P),$$

$$\mathbf{\Phi}^{(j)}(P) = \mathbf{U}^{(j)}(P)\mathbf{X}^{(j)}(P).$$
(30)

With the initial condition  $\tilde{\boldsymbol{T}}_{\mathrm{DMD}}(t^{(0)}(P);P) = \boldsymbol{T}^{(0)}(P)$ , the DMD prediction  $\tilde{\boldsymbol{T}}_{\mathrm{DMD}}(t;P)$  is then given by: iteratively for  $1 \leq j \leq J$ , for  $t \in [\tau^{(j-1)}(P),\tau^{(j)}(P)]$ ,

$$\widetilde{\boldsymbol{T}}_{\text{DMD}}(t;P) = \boldsymbol{\Phi}^{(j)}(P) \left[ \boldsymbol{\Lambda}^{(j)}(P) \right]^{\frac{t-\tau^{(j-1)}(P)}{\Delta t}} \left[ \boldsymbol{\Phi}^{(j)}(P) \right]^{\dagger}$$

$$\widetilde{\boldsymbol{T}}_{\text{DMD}}(\tau^{(j-1)}(P);P),$$
(31)

where  $\widetilde{T}_{\text{DMD}}(\tau^{(j-1)}; P)$  is set to be the initial state  $T^{(0)}(P)$  if j = 1, and is obtained from DMD approximation in the previous time subinterval for j > 1.

As a final remark, for all  $1 \leq i \leq N_P$ , we have  $i_{\text{ref}}(P_i) = i$ , which implies  $\mathbf{Q}_i^{(j)}(P_i) = \mathbf{I}_{r_j}$ . Thanks to (22), we have  $\tau^{(j)}(P_i) = \tau_i^{(j)}$  for all  $0 \leq j \leq J$ , and  $\mathbf{U}^{(j)}(P_i) = \mathbf{U}_i^{(j)}$  and  $\widehat{\mathbf{A}}^{(j)}(P_i) = \widehat{\mathbf{A}}_i^{(j)}$  for all  $1 \leq j \leq J$ . Therefore, (31) actually reproduces (19) at the training shock pressures  $P_i \in \mathcal{D}_{\text{train}}$ .

### 5 Continuous conditional generative adversarial network

Generative adversarial network (GAN) was introduced in [79] as a deep learning method that learns a parametrized representation by random latent codes for a set of training data in an unsupervised manner and allows fast sampling from the distribution represented by the dataset. In the original work [79], GAN formulates a two-player minimax game with a binary classification score as an optimization problem, and trains two artificial neural networks, the discriminator and the generator, simultaneously to optimize the objective function in opposing ways. These networks compete with each other, with one aiming to maximize the objective function and the other aiming to minimize it. In [80], deep convolutional generative adversarial network (DCGAN) is developed by for image generation tasks by utilizing deep convolutional architectures in GAN. GANs have been successfully applied to different scientific applications, including subsurface applications in porous media [62], geological modeling in [81, 82], and geostatistical inversion in [83].

In this section, we introduce a GAN-based dynamical prediction scheme for the numerical simulation data. Our method is based on residual network structure and modified from [62] which adopts several recent improvements to GAN, including batch-based critic architecture [84] and U-Net generator architecture [85] in pix2pix [86] for the image-to-image translation task, earth mover distance as loss function in Wasserstein GAN [87], and continuous conditional generator input [88]. In Section 5.1, we will discuss the details of the neural network. In Section 5.2, we will introduce the predictive procedure of GAN on generic shock pressure  $P \in D$ , which is in general unseen in the training samples.

### 5.1 Offline stage

We begin the discussion of the offline procedure in the continuous conditional generative adversarial network (CcGAN) approach with data preprocessing. We represent the sampled data of the temperature fields  $T_i^{(k)}$  as matrices in  $\mathbb{R}^{N_x \times N_x}$ , and define the residual as

$$R_i^{(k)} = T_i^{(k+1)} - T_i^{(k)} \in \mathbb{R}^{N_x \times N_x}.$$
 (32)

The training data are normalized by: for  $1 \le i \le N_P$  and  $0 \le k < m$ ,

$$\overline{t}^{(k)} = k/(m-1) \in [0,1],$$

$$\overline{P}_i = (P_i - P_{\min})/(P_{\max} - P_{\min}) \in [0,1],$$

$$\overline{T}_i^{(k)} = \overline{T}_i^{(k)}/(T_{\max} - T_{\min}) \in [0,1]^{N_x \times N_x},$$

$$\overline{R}_i^{(k)} = R_i^{(k)}/(RSymbol_{\max} - RSymbol_{\min}) \in [0,1]^{N_x \times N_x},$$
(33)

where

$$T_{\text{max}} = \max_{1 \le i \le N_P, 0 \le k < m} \boldsymbol{T}_i^{(k)},$$

$$T_{\text{in}} = \max_{1 \le i \le N_P, 0 \le k < m} \boldsymbol{T}_i^{(k)},$$

$$\boldsymbol{RSymbol_{\text{max}}} = \max_{1 \le i \le N_P, 0 \le k < m} \boldsymbol{R}_i^{(k)},$$

$$\boldsymbol{RSymbol_{\text{in}}} = \max_{1 \le i \le N_P, 0 \le k < m} \boldsymbol{R}_i^{(k)}.$$
(34)

Then the labelled paired training dataset is given by

$$S_{\text{in}} = \left\{ \left( \overline{t}^{(k)}, \overline{P}_i, \overline{T}_i^{(k)} \right) : 1 \le i \le N_P \text{ and } 0 \le k < m \right\},$$

$$S_{\text{out}} = \left\{ \overline{R}_i^{(k)} : 1 \le i \le N_P \text{ and } 0 \le k < m \right\},$$
(35)

Given the normalized datasets  $(S_{\rm in}, S_{\rm out})$ , the goal is to learn a generator  $G^{\star}$ :  $\mathbb{R} \times \mathbb{R} \times \mathbb{R}^{N_x \times N_x} \to [0, 1]^{N_x \times N_x}$  which approximates the discrete dynamics

$$\overline{\boldsymbol{R}}_i^{(k)} \approx G^\star\left(\overline{\boldsymbol{t}}^{(k)}, \overline{\boldsymbol{P}}_i, \overline{\boldsymbol{T}}_i^{(k)}\right) \text{ for all } 1 \leq i \leq N_P \text{ and } 0 \leq k < m.$$

In the GAN framework, the generator  $G^*$  is learnt through optimizing the function G to minimize a objective functional which measures the distance of the generator distribution and the groundtruth distribution in a certain metric. The generator G is set to compete with another neural network  $D: \mathbb{R} \times \mathbb{R} \times \mathbb{R}^{N_x \times N_x} \to \mathbb{R}$ , called the critic. The two functions have opposite objectives, as the critic aims to distinguish the generator distribution from the groundtruth distribution, while the generator aims to fool the discriminator. In our work, the overall objective has three components. First, we use the earth mover distance in [87], as the competing objective, which is formally defined as

$$\mathcal{L}_{\text{WGAN}}(D,G) = \sum_{i=1}^{N_P} \sum_{k=0}^{m-1} D\left(\overline{t}^{(k)}, \overline{P}_i, \overline{R}_i^{(k)}\right) - D\left(\overline{t}^{(k)}, \overline{P}_i, G\left(\overline{t}^{(k)}, \overline{P}_i, \overline{T}_i^{(k)}\right)\right).$$
(36)

Second, we use the gradient penalty in [89] as a regularizer to weakly enforce the 1-Lipschitz continuity in the critic, which is given by

$$\mathcal{L}_{\text{Lip}}(D) = \sum_{i=1}^{N_P} \sum_{k=0}^{m-1} \left( \left\| \nabla_{\overline{T}} D\left(\overline{t}^{(k)}, \overline{P}_i, \varepsilon_i^{(k)} \overline{R}_i^{(k)} + (1 - \varepsilon_i^{(k)}) G\left(\overline{t}^{(k)}, \overline{P}_i, \overline{T}_i^{(k)}\right) \right) \right\|_2 - 1 \right)^2,$$
(37)

where  $\varepsilon_i^{(k)} \sim \mathcal{U}(0,1)$  is independent and identically distributed. Third, we use the absolute distance as the reconstruction objective, which is defined as

$$\mathcal{L}_{\text{recon}}(G) = \sum_{i=1}^{N_P} \sum_{k=0}^{m-1} \left| \overline{R}_i^{(k)} - G\left(\overline{t}^{(k)}, \overline{P}_i, \overline{T}_i^{(k)}\right) \right|. \tag{38}$$

The optimization problem is then formulated as

$$\min_{G \in \mathcal{G}} \max_{D \in \mathcal{D}} \mathcal{L}_{\text{WGAN}}(D, G) + \mu_{\text{Lip}} \mathcal{L}_{\text{Lip}}(D) + \mu_{\text{recon}} \mathcal{L}_{\text{recon}}(G), \tag{39}$$

where  $\mu_{\text{Lip}} > 0$  and  $\mu_{\text{recon}} > 0$  are regularization parameters which control the tradeoff between the three components in the overall objective,  $\mathcal{G}$  is a class of neural networks with the U-Net architecture, and  $\mathcal{D}$  is a class of convolutional neural networks. The generator and the critic are trained simultaneously and the objective functional is dynamic to each of them in the training process. In our work, we use the adaptive moment estimation (ADAM) method [90] to update the critic D and the generator Gin alternating direction.

### 5.2 Prediction stage

After sufficient training, the generator  $G^*$  can serve as a global surrogate model for predicting the temperature field. At a generic shock pressure  $P \in \mathsf{D}$ , with the initial condition  $\widetilde{T}_{\mathrm{GAN}}(t^{(0)}(P);P) = T^{(0)}(P)$ , for  $0 \leq k < m$ , the GAN prediction  $\widetilde{T}_{\mathrm{GAN}}(t^{(k+1)}(P);P) \in \mathbb{R}^{N_x \times N_x}$  is iteratively given by

$$\widetilde{\boldsymbol{T}}_{\text{GAN}}(t^{(k+1)}(P); P) = \widetilde{\boldsymbol{T}}_{\text{GAN}}(t^{(k)}(P); P) + (R_{\text{max}} - R_{\text{min}})G^{\star}\left(\overline{t}^{(k)}, \overline{P}, \overline{\boldsymbol{T}}_{\text{GAN}}^{(k)}(P)\right),$$

$$(40)$$

where

$$\overline{P} = (P - P_{\min})/(P_{\max} - P_{\min}),$$

$$\overline{T}_{GAN}^{(k)}(P) = \widetilde{T}_{GAN}(t^{(k)}(P); P)/(T_{\max} - T_{\min}).$$
(41)

### 6 Numerical experiments

In this section, we present some numerical results to test the performance of our proposed methods when applied to the numerical simulation data for the pore collapse process.

### 6.1 Problem specification

In our numerical experiments, the bounds of the range D of applied shock pressure are  $P_{\min} = 11$  and  $P_{\max} = 15$ , and the spatial region of interest  $\Omega_{\text{obs}}$  is a square which is partitioned into  $N_x^2 = 128^2$  square sub-zones with equal length  $h_x = 25$ . In order to

depict the pore collapse process, explained in Figure 1, we choose m=180,  $\Delta t=2.5$ , and  $t^{(0)}(P)=0.9875-0.0125P$ , as the initial time of the time interval of interest  $\mathcal{T}(P)$  for the shock pressure  $P\in D$ . Figure 3 depicts some selected representative snapshots of temperature fields at different shock pressures ranging from 11 to 15 GPa, in the corresponding time interval of interest. Each row corresponds to the same shock pressure. Unlike Figure 3, the snapshots in the same column do not correspond to the same time instance.

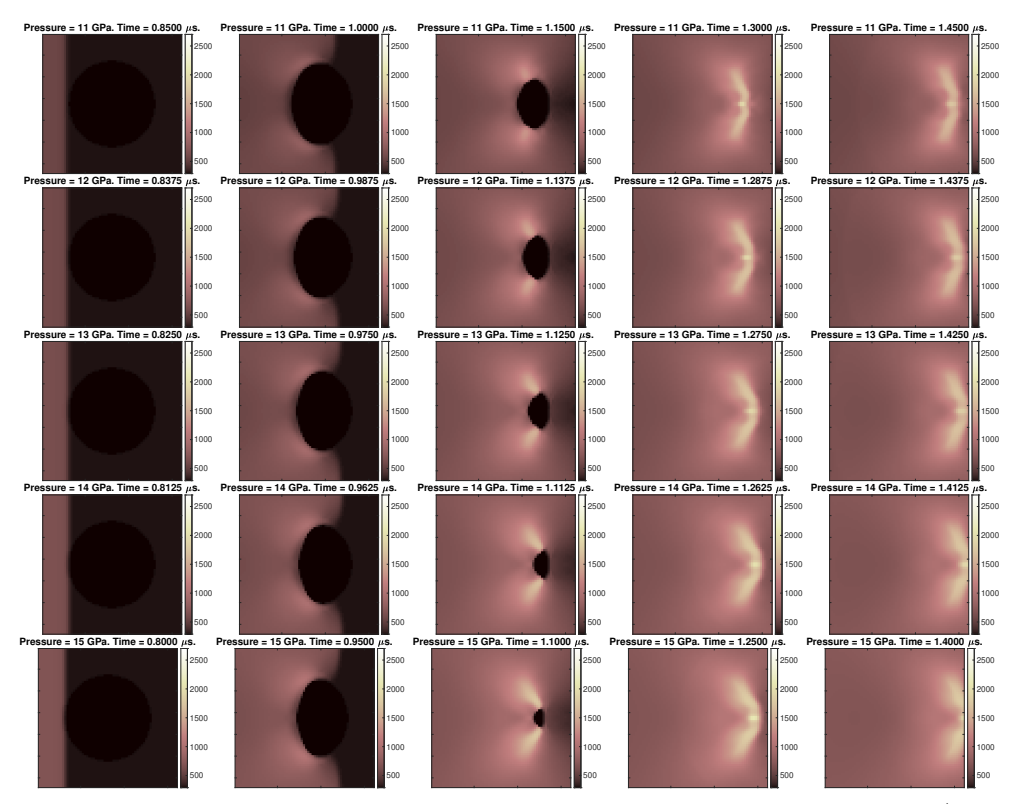


Fig. 4 Selected representative snapshots of temperature fields at different shock pressures (11-15 GPa, row-wise) in the corresponding time interval of interest, which is adjusted to depict the pore collapse process. Unlike Figure 3, the snapshots in the same column do not correspond to same time instance.

### 6.2 Methodology specification

In this subsection, we discuss the details of the surrogate modeling approaches in performing the numerical experiments.

We first discuss the details about DMD in Section 4. We use the DW-DMD approach described in Section 4.2. with J=20 and  $r_j\equiv 9$ , and we use Gaussian

functions in RBF interpolation. All the DMD results are generated using the implementation in libROM <sup>1</sup> on Quartz in Livermore Computing Center<sup>2</sup>, on Intel Xeon CPUs with 128 GB memory, peak TFLOPS of 3251.4, and peak single CPU memory bandwidth of 77 GB/s. The training of each local DMD model takes around 30 seconds on CPU.

Next, we discuss the details about CcGAN in Section 5. The U-Net generator architecture is presented in Figure 5. Following [62], we take  $\mu_{\rm Lip} = 10$  and  $\mu_{\rm recon} = 500$ in the objective (39). All the CcGAN results are generated on Lassen in Livermore Computing Center<sup>3</sup>, on Intel Power9 CPUs with 256 GB memory and NVIDIA V100 GPUs, peak TFLOPS of 23,047.20, and peak single CPU memory bandwidth of 170 GB/s. With a batch size 6 and 2000 epoches, the training of global CcGAN model takes 8 hours on GPU.

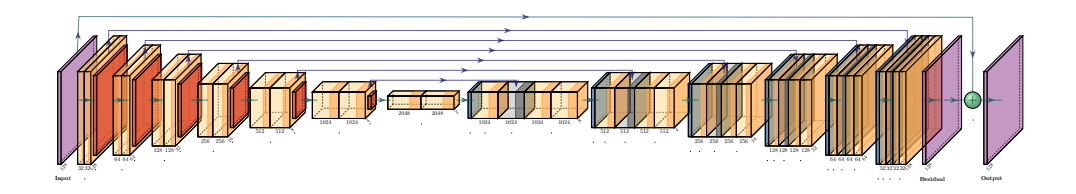


Fig. 5 U-Net generator architecture used in the examples presented in Section 6.

### 6.3 Prediction and performance evaluation

In the remaining of this section, we will present numerical results with various training combinations of surrogate modeling approaches and training shock pressures D<sub>train</sub>. In Figure 6, we show the comparison of some selected groundtruth snapshots and the corresponding surrogate model approximations at P=12, with each row corresponds to:

- 1. groundtruth snapshots from simulation data,
- 2. reproductive predictions with local DW-DMD and  $D_{\text{train}} = \{12\},\$
- 3. interpolatory predictions with parametric DW-DMD and  $D_{train} = \{11, 13, 15\},\$
- 4. extrapolatory predictions with local DW-DMD and  $D_{train} = \{13\},\$
- 5. reproductive predictions with local CcGAN and  $D_{\text{train}} = \{12\}$
- 6. reproductive predictions with global CcGAN and  $D_{train} = \{12, 14\},\$
- 7. interpolatory predictions with global CcGAN and  $D_{train} = \{11, 13, 15\}$ , and
- 8. extrapolatory predictions with local CcGAN and  $D_{\text{train}} = \{13\},\$

and each column corresponds to a time instance  $t_k(P) \in \mathcal{T}(P)$ , with  $k \in$ {10, 50, 90, 130, 170}, in the time interval of query. The reproductive cases will be further explained in Section 6.4, and the interpolatory and extrapolatory cases will be

<sup>&</sup>lt;sup>1</sup>GitHub page, https://github.com/LLNL/libROM.

<sup>&</sup>lt;sup>2</sup>High performance computing at LLNL, https://hpc.llnl.gov/hardware/platforms/quartz 
<sup>3</sup>High performance computing at LLNL, https://hpc.llnl.gov/hardware/platforms/lassen

further explained in Section 6.5. It can be seen that the approximations from DMD, in the second row to the fourth row, in general better captures the pore collapse process and resembles the simulation data in the first row.

Next, we will introduce some performance metric which allows us to investigate and compare the methods and training combination further. To evaluate the accuracy of the prediction, we compute the relative error between the high-fidelity simulation data T and the reduced order model approximation  $\tilde{T}$ , i.e.,  $\tilde{T}_{\text{DMD}}$  or  $\tilde{T}_{\text{GAN}}$ , at testing shock pressure  $P \in \mathbb{D}$  and time instance  $t \in \tilde{\mathcal{T}}(P)$  by:

$$\varepsilon(t; P) = \frac{\|T(t; P) - \widetilde{T}(t; P)\|}{\|T(t; P)\|},$$

where  $\|\cdot\|$  denotes the vector Euclidean norm in  $\mathbb{R}^{N_x^2}$ , or equivalently the matrix Frobenius norm in  $\mathbb{R}^{N_x \times N_x}$ .

### 6.4 Reproductive cases

As a first experiment, we test the accuracy of surrogate modeling approaches in reproductive cases, where the testing shock pressure is identical to that used in one of the training shock pressures, i.e.,  $P \in D_{\text{train}}$ .

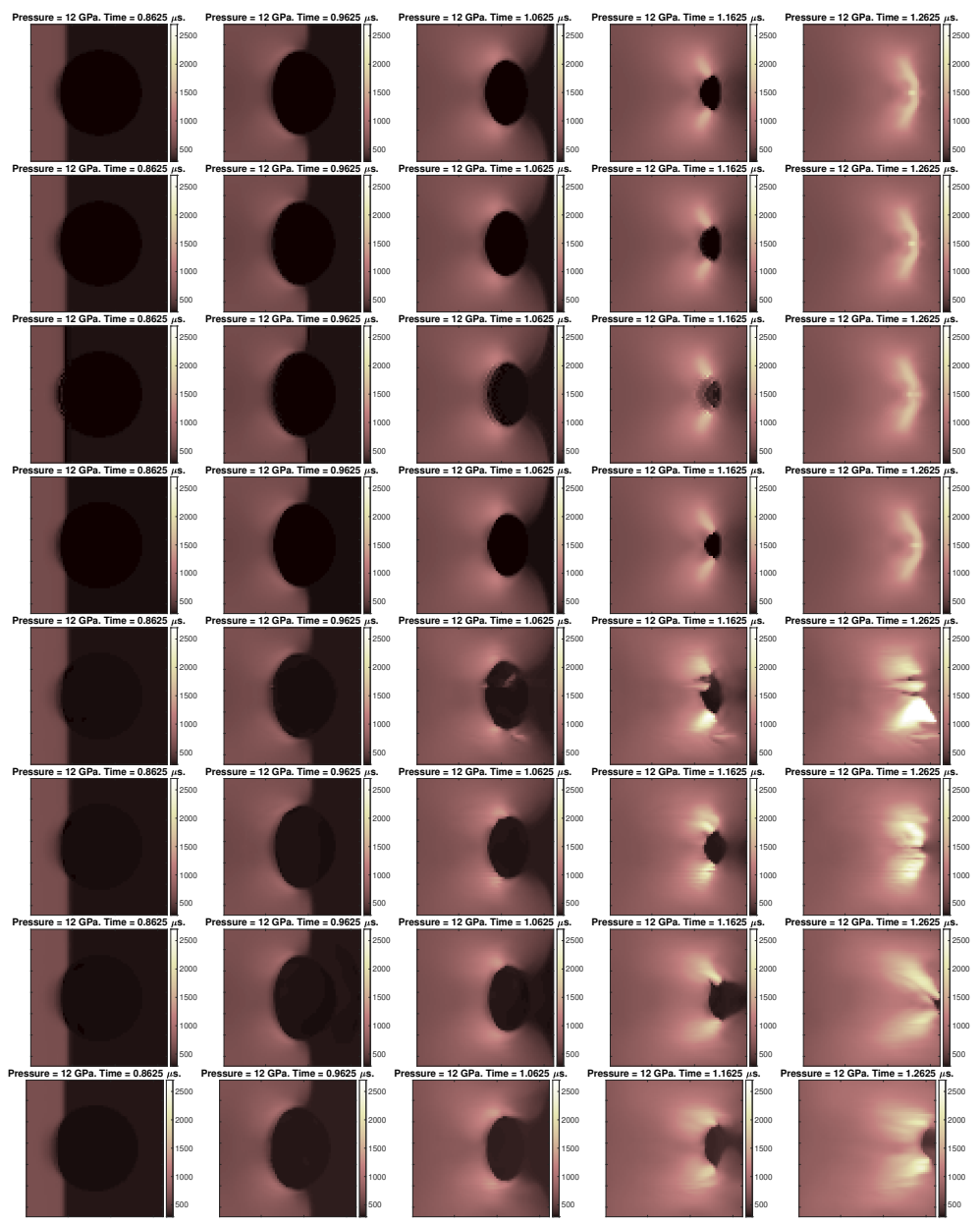
Figure 7 shows the comparison of reproductive accuracy using local DW-DMD and local CcGAN, in terms of the evolution of relative error (in logarithmic scale), with  $D_{\rm train} = \{12\}$  and  $D_{\rm train} = \{13\}$  respectively. In both cases, local DW-DMD produces more stable reproductive results, where the relative error stays below 1.2% in the whole time interval of query, and terminates at around 0.3% at final time. On the other hand, although local CcGAN is able to produce around 0.2% error in each time step, the error accumulates quickly and rises to 32% and 22% at the final time of query with  $D_{\rm train} = \{12\}$  and  $D_{\rm train} = \{13\}$  respectively.

Figure 8 shows a similar comparison with  $D_{\rm train} = \{12,14\}$  and  $D_{\rm train} = \{11,13,15\}$  respectively. We remark that the final-time error of DMD at the reproductive cases remains unchanged at around 0.3% when adding more training shock pressures, as explained in Section 4.3. On the other hand, the final-time error of global CcGAN improves to 16% with  $D_{\rm train} = \{12,14\}$  and remains at 22% with  $D_{\rm train} = \{11,13,15\}$  respectively.

### 6.5 Predictive cases

In this subsection, we test the accuracy of surrogate modeling approaches in predictive cases, where the testing shock pressure is not one of the training shock pressures, i.e.,  $P \in \mathsf{D} \setminus \mathsf{D}_{\mathrm{train}}$ .

We begin with some results in the interpolatory cases, i.e.,  $P \in (\min \mathsf{D}_{\mathsf{train}}, \max \mathsf{D}_{\mathsf{train}}) \setminus \mathsf{D}_{\mathsf{train}}$ . Similar to Figure 8, we compare the relative error at P = 12 with  $\mathsf{D}_{\mathsf{train}} = \{11, 13, 15\}$ , and at P = 13 with  $\mathsf{D}_{\mathsf{train}} = \{11, 13, 15\}$  respectively. In the former case, the relative error of parametric DW-DMD is higher than that of global CcGAN in an earlier stage, but eventually becomes lower. Throughout the whole time interval of query, the relative error of parametric DW-DMD stays



**Fig. 6** Selected snapshots and predictions of temperature fields at 12GPa. Each row corresponds to: 1. groundtruth snapshots from simulation data, 2. local DW-DMD and  $D_{\rm train} = \{12\}$ , 3. parametric DW-DMD and  $D_{\rm train} = \{11, 13, 15\}$ , 4. local DW-DMD and  $D_{\rm train} = \{13\}$ , 5. local CcGAN and  $D_{\rm train} = \{12\}$ , 6. global CcGAN and  $D_{\rm train} = \{12, 14\}$ , 7. global CcGAN and  $D_{\rm train} = \{11, 13, 15\}$ , and 8. local CcGAN and  $D_{\rm train} = \{13\}$ .

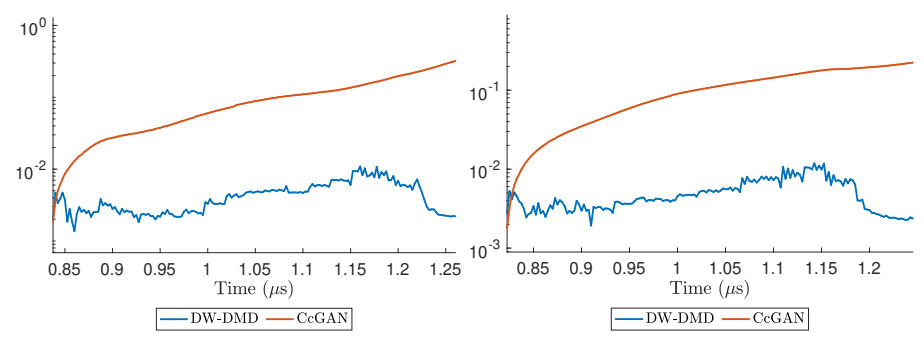


Fig. 7 Relative error (in logarithmic scale) of reproductive cass at testing shock pressure P=12 with  $D_{\rm train}=\{12\}$  (left), and at testing shock pressure P=13 with  $D_{\rm train}=\{13\}$  (right), using local DW-DMD (in blue) and local CcGAN (in red).

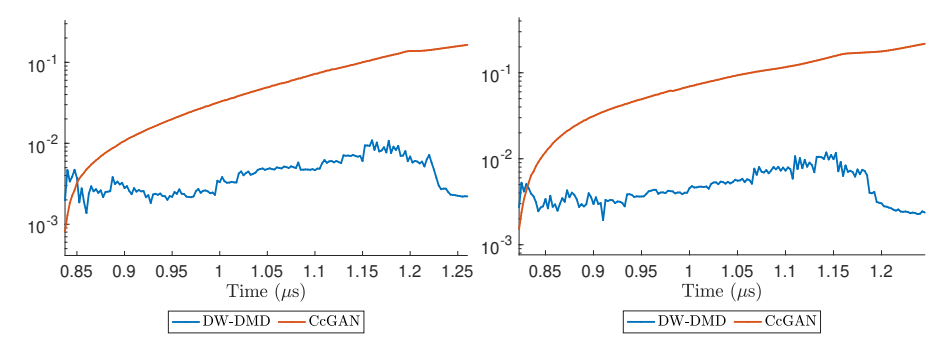


Fig. 8 Relative error (in logarithmic scale) of reproductive cases at testing shock pressure P=12 with  $D_{\rm train}=\{12,14\}$  (left), and at testing shock pressure P=13 with  $D_{\rm train}=\{11,13,15\}$  (right), using parametric DW-DMD (in blue) and global CcGAN (in red).

below 9% and 4.3% and terminates at around 4.7% and 1.3% at final time, in the former and the latter case respectively. Meanwhile, the relative error of global CcGAN accumulates to 20% at the final time of query in both cases.

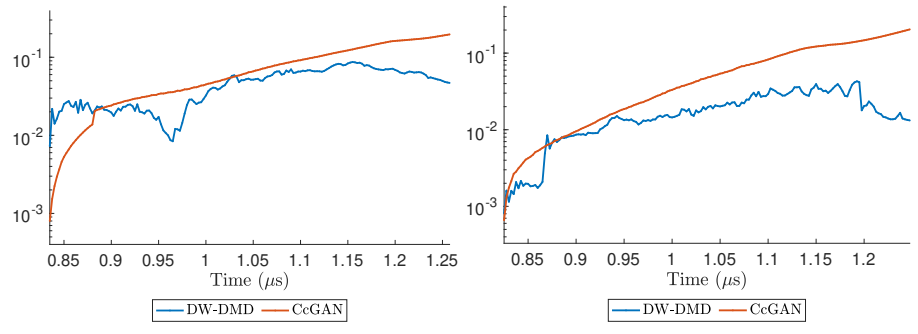


Fig. 9 Relative error (in logarithmic scale) of interpolatory cases at testing shock pressure P=12 with  $D_{train}=\{11,13,15\}$  (left), and at testing shock pressure P=13 with  $D_{train}=\{12,14\}$  (right), using parametric DW-DMD (in blue) and global CcGAN (in red).

Next, we will present some results in extrapolatory cases, i.e.,  $P \in D \setminus (\min D_{\text{train}}, \max D_{\text{train}})$ . Figure 10 shows the comparison of extrapolatory accuracy at P=15 using local DW-DMD and local CcGAN, in terms of the relative error of the temperature field over time, with  $D_{\text{train}}=\{12\}$  and  $D_{\text{train}}=\{13\}$  respectively. The relative error of DW-DMD attains a maximum of 15% and 12% over time and terminates at 10% and 7% at final time with  $D_{\text{train}}=\{12\}$  and  $D_{\text{train}}=\{13\}$  respectively. Meanwhile, the relative error of CcGAN attains the maximum 15% and 23% at the final time, with  $D_{\text{train}}=\{12\}$  and  $D_{\text{train}}=\{13\}$  respectively. Unlike the DW-DMD results which shows the extrapolatory accuracy deteriorates as the testing shock pressure is farther away from the training shock pressure, the extrapolatory accuracy of CcGAN is unstable with the distance between testing shock pressure P and the training shock pressure P1.

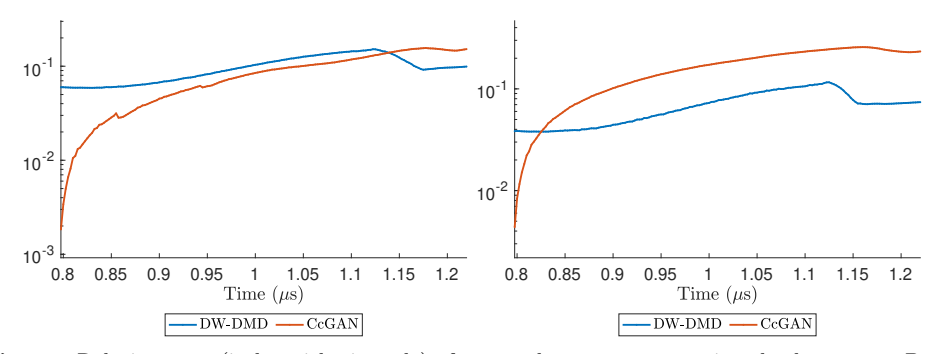


Fig. 10 Relative error (in logarithmic scale) of extrapolatory case at testing shock pressure P=15 with  $D_{\rm train}=\{12\}$  (left) and  $D_{\rm train}=\{13\}$  (right), using local DW-DMD (in blue) and CcGAN (in red).

Figure 11 shows the comparison of reproductive and extrapolatory accuracy at various testing shock pressure  $P \in \{11, 12, 13, 14, 15\}$  in terms of the relative error of the temperature field at the final time of query, using local DW-DMD and local CcGAN with respect to different training shock pressure  $P_1 \in D_{\text{train}}$ . It can be observed that with DW-DMD, the relative error at the reproductive case is always around 0.3%, while the error at the extrapolatory case increases as the testing shock pressure is farther away from the training shock pressure, which is a common phenomenon for parametric reduced order models. The relative error attains the maximum of 12%, when  $|P - P_1| = 4$ , in our testing cases. Meanwhile, the error with CcGAN is always above 10% and unstable with the distance between testing shock pressure P and the training shock pressure  $P_1$ . With  $D_{\text{train}} = \{12\}$ , the relative error goes up to 45% at P = 14.

Figure 12 shows the comparison of reproductive, interpolatory and extrapolatory accuracy at various testing shock pressure  $P \in \{11, 12, 13, 14, 15\}$  in terms of the relative error of the temperature field at the final time of query, using parametric DW-DMD with  $12 \in D_{\text{train}}$  and  $13 \in D_{\text{train}}$  respectively. The error at the newly added training shock pressures is also reduced to around 0.3%, and the error at the predictive

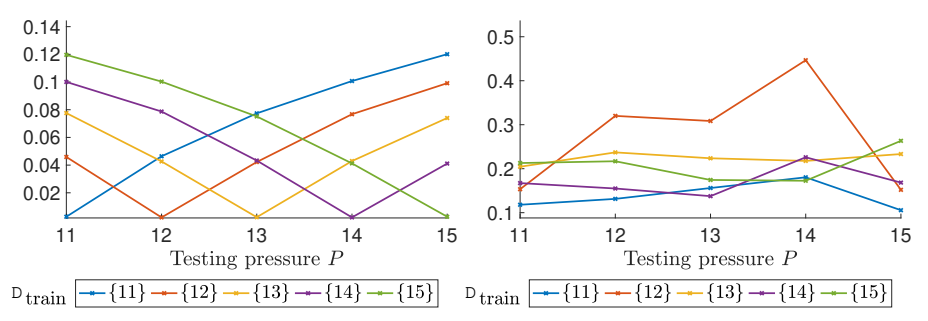


Fig. 11 Relative error at various testing shock pressures, using local DW-DMD (left) and CcGAN (right) with various training shock pressure in  $D_{\rm train}$ .

cases are also reduced in general, which ranges from 1.3% to 5% in the interpolatory cases and 8% to 9% in extrapolatory cases.

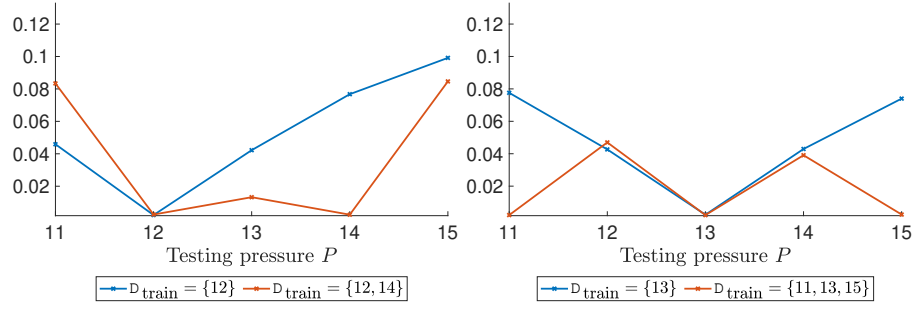


Fig. 12 Relative error at various testing shock pressures, using parametric DW-DMD with  $12 \in D_{\text{train}}$  (left) and  $13 \in D_{\text{train}}$  (right).

Figure 13 shows a similar comparison using global CcGAN. While adding more training shock pressures and enriching the training datasets in global CcGAN makes an improvement in the overall solution accuracy, the error is always around 20%, which is still a lot higher than the parametric DW-DMD by comparing to the same case in Figure 12.

### 7 Conclusion

In this paper, we propose two data-driven surrogate modeling approaches for computationally economical prediction of complex physics phenomena in shock-induced pore collapse processes. The surrogate models are built based on dynamic mode decomposition and U-Net generative adversarial networks, and modified to overcome the challenges of data scarcity and pressure-dependent advective and transport dynamics. The shock pressure is incorporated in the construction of the surrogate models, by means of parametric interpolation in dynamic mode decomposition and conditional input in generative adversarial networks, respectively. Moreover, windowing is

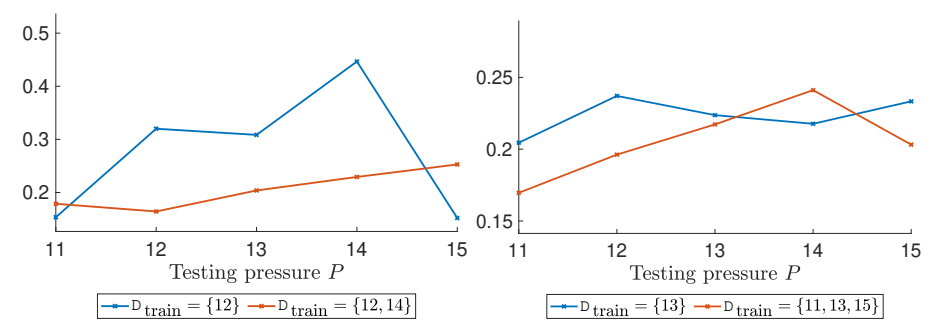


Fig. 13 Relative error at various testing shock pressures, using global CcGAN with  $12 \in D_{\text{train}}$  (left) and  $13 \in D_{\text{train}}$  (right).

used in dynamic mode decomposition for efficient dimensionality reduction by further localizing reduced order models in time.

In our numerical realization of these surrogate models, the training of dynamic mode composition is much more efficient than generative adversarial network. Moreover, dynamic mode decomposition produces more stable approximation and accurate prediction for the whole pore collapse processes at unseen shock pressures. Although the generative model was outperformed by dynamic mode decomposition in this study, it will be interesting to see how the advances of cutting-edge neural network approaches can make improvements in efficiency and accuracy to dynamic surrogate modeling of data-scarce large-scale applications with advective and transport phenomena like pore collapse processes. In the meantime, some physics-guided data-driven approach with simpler machine learning methods, like the local distance windowing dynamic mode decomposition, will serve as a powerful tool for these applications. In our future research plan, we will expand our study to encompass higher pressure regimes and post-collapse mechanisms.

### Acknowledgments

This work was performed at Lawrence Livermore National Laboratory and supported by the LLNL-LDRD Program under Project No. 24-SI-004. Lawrence Livermore National Laboratory is operated by Lawrence Livermore National Security, LLC, for the U.S. Department of Energy, National Nuclear Security Administration under Contract DE-AC52-07NA27344 and LLNL-JRNL-849281.

### Disclaimer

This document was prepared as an account of work sponsored by an agency of the United States government. Neither the United States government nor Lawrence Livermore National Security, LLC, nor any of their employees makes any warranty, expressed or implied, or assumes any legal liability or responsibility for the accuracy, completeness, or usefulness of any information, apparatus, product, or process disclosed, or represents that its use would not infringe privately owned rights. Reference herein to any specific commercial product, process, or service by trade name,

trademark, manufacturer, or otherwise does not necessarily constitute or imply its endorsement, recommendation, or favoring by the United States government or Lawrence Livermore National Security, LLC. The views and opinions of authors expressed herein do not necessarily state or reflect those of the United States government or Lawrence Livermore National Security, LLC, and shall not be used for advertising or product endorsement purposes.

This article has been authored by an employee of National Technology & Engineering Solutions of Sandia, LLC under Contract No. DE-NA0003525 with the U.S. Department of Energy (DOE). The employee owns all right, title and interest in and to the article and is solely responsible for its contents. Sandia National Laboratories is a multimission laboratory managed and operated by National Technology and Engineering Solutions of Sandia LLC, a wholly owned subsidiary of Honeywell International Inc. for the U.S. Department of Energy's National Nuclear Security Administration under contract DE-NA0003525. This paper describes objective technical results and analysis. Any subjective views or opinions that might be expressed in the paper do not necessarily represent the views of the U.S. Department of Energy or the United States Government.

### References

- [1] Tong, W., Ravichandran, G.: Dynamic pore collapse in viscoplastic materials. Journal of applied physics **74**(4), 2425–2435 (1993) https://doi.org/10.1063/1.354678
- [2] Erhart, P., Bringa, E.M., Kumar, M., Albe, K.: Atomistic mechanism of shock-induced void collapse in nanoporous metals. Physical Review B 72(5), 052104 (2005) https://doi.org/10.1103/PhysRevB.72.052104
- [3] Schade, S., Wünnemann, K.: Numerical modeling of pore space collapse due to shock wave compression. In: 38th Annual Lunar and Planetary Science Conference, Houston, TX, p. 2029 (2007). https://www.lpi.usra.edu/meetings/lpsc2007/ pdf/2029.pdf
- [4] Adhikari, U., Goliaei, A., Berkowitz, M.L.: Mechanism of membrane poration by shock wave induced nanobubble collapse: A molecular dynamics study. The Journal of Physical Chemistry B 119(20), 6225–6234 (2015) https://doi.org/10. 1021/acs.jpcb.5b02218
- [5] Dattelbaum, D.M., Coe, J.D.: Shock-driven decomposition of polymers and polymeric foams. Polymers 11(3), 493 (2019) https://doi.org/10.3390/ polym11030493

### //doi.org/10.2172/1361589

- [7] Berkooz, G., Holmes, P., Lumley, J.L.: The proper orthogonal decomposition in the analysis of turbulent flows. Annual review of fluid mechanics **25**(1), 539–575 (1993) https://doi.org/10.1146/annurev.fl.25.010193.002543
- [8] Safonov, M.G., Chiang, R.: A Schur method for balanced-truncation model reduction. IEEE Transactions on Automatic Control 34(7), 729–733 (1989) https://doi.org/10.1109/9.29399
- [9] Rozza, G., Huynh, D.B.P., Patera, A.T.: Reduced basis approximation and a posteriori error estimation for affinely parametrized elliptic coercive partial differential equations: application to transport and continuum mechanics. Archives of Computational Methods in Engineering 15(3), 229 (2008) https://doi.org/10. 1007/s11831-008-9019-9
- [10] Lee, K., Carlberg, K.T.: Model reduction of dynamical systems on nonlinear manifolds using deep convolutional autoencoders. Journal of Computational Physics 404, 108973 (2020) https://doi.org/10.1016/j.jcp.2019.108973
- [11] Maulik, R., Lusch, B., Balaprakash, P.: Reduced-order modeling of advection-dominated systems with recurrent neural networks and convolutional autoencoders. Physics of Fluids **33**(3), 037106 (2021) https://doi.org/10.1063/5.0039986
- [12] Kim, Y., Choi, Y., Widemann, D., Zohdi, T.: A fast and accurate physics-informed neural network reduced order model with shallow masked autoencoder. Journal of Computational Physics **451**, 110841 (2022) https://doi.org/10.1016/j.jcp.2021. 110841
- [13] Gugercin, S., Antoulas, A.C.: A survey of model reduction by balanced truncation and some new results. International Journal of Control **77**(8), 748–766 (2004) https://doi.org/10.1080/00207170410001713448
- [14] Benner, P., Gugercin, S., Willcox, K.: A survey of projection-based model reduction methods for parametric dynamical systems. SIAM review **57**(4), 483–531 (2015) https://doi.org/10.1137/130932715
- [15] Choi, Y., Carlberg, K.: Space-time least-squares Petrov-Galerkin projection for nonlinear model reduction. SIAM Journal on Scientific Computing 41(1), 26–58 (2019) https://doi.org/10.1137/17M1120531
- [16] Choi, Y., Coombs, D., Anderson, R.: SNS: a solution-based nonlinear subspace method for time-dependent model order reduction. SIAM Journal on Scientific Computing 42(2), 1116–1146 (2020) https://doi.org/10.1137/19M1242963

- [17] Carlberg, K., Choi, Y., Sargsyan, S.: Conservative model reduction for finite-volume models. Journal of Computational Physics **371**, 280–314 (2018) https://doi.org/10.1016/j.jcp.2018.05.019
- [18] Xiao, D., Fang, F., Buchan, A.G., Pain, C.C., Navon, I.M., Du, J., Hu, G.: Non-linear model reduction for the Navier–Stokes equations using residual DEIM method. Journal of Computational Physics 263, 1–18 (2014) https://doi.org/10. 1016/j.jcp.2014.01.011
- [19] Burkardt, J., Gunzburger, M., Lee, H.-C.: POD and CVT-based reduced-order modeling of Navier-Stokes flows. Computer methods in applied mechanics and engineering 196(1-3), 337-355 (2006) https://doi.org/10.1016/j.cma.2006.04.004
- [20] Copeland, D.M., Cheung, S.W., Huynh, K., Choi, Y.: Reduced order models for lagrangian hydrodynamics. Computer Methods in Applied Mechanics and Engineering 388, 114259 (2022) https://doi.org/10.1016/j.cma.2021.114259
- [21] Cheung, S.W., Choi, Y., Copeland, D.M., Huynh, K.: Local Lagrangian reducedorder modeling for Rayleigh-Taylor instability by solution manifold decomposition. Journal of Computational Physics 472, 111655 (2023) https://doi.org/10. 1016/j.jcp.2022.111655
- [22] Ghasemi, M., Gildin, E.: Localized model reduction in porous media flow. IFAC-PapersOnLine 48(6), 242–247 (2015) https://doi.org/j.ifacol.2015.08.038
- [23] Cheung, S.W., Chung, E.T., Efendiev, Y., Leung, W.T., Vasilyeva, M.: Constraint energy minimizing generalized multiscale finite element method for dual continuum model. Communications in Mathematical Sciences 18(3), 663–685 (2020) https://doi.org/10.4310/CMS.2020.v18.n3.a4
- [24] Zhao, P., Liu, C., Feng, X.: POD-DEIM based model order reduction for the spherical shallow water equations with Turkel-Zwas finite difference discretization. Journal of Applied Mathematics 2014 (2014) https://doi.org/10.1155/2014/ 292489
- [25] Ştefănescu, R., Navon, I.M.: POD/DEIM nonlinear model order reduction of an ADI implicit shallow water equations model. Journal of Computational Physics 237, 95–114 (2013) https://doi.org/10.1016/j.jcp.2012.11.035
- [26] Choi, Y., Brown, P., Arrighi, B., Anderson, R., Huynh, K.: Space-time reduced order model for large-scale linear dynamical systems with application to Boltzmann transport problems. Journal of Computational Physics 424, 109845 (2021) https://doi.org/10.1016/j.jcp.2020.109845
- [27] Fares, M., Hesthaven, J.S., Maday, Y., Stamm, B.: The reduced basis method for the electric field integral equation. Journal of Computational Physics **230**(14), 5532–5555 (2011) https://doi.org/10.1016/j.jcp.2011.03.023

- [28] Cheng, M.-C.: A reduced-order representation of the Schrödinger equation. AIP Advances **6**(9), 095121 (2016) https://doi.org/10.1063/1.4963835
- [29] Cheung, S.W., Chung, E.T., Efendiev, Y., Leung, W.T.: Explicit and energy-conserving constraint energy minimizing generalized multiscale discontinuous galerkin method for wave propagation in heterogeneous media. Multiscale Modeling & Simulation 19(4), 1736–1759 (2021) https://doi.org/10.1137/20M1363832
- [30] Washabaugh, K., Amsallem, D., Zahr, M., Farhat, C.: Nonlinear model reduction for CFD problems using local reduced-order bases. In: 42nd AIAA Fluid Dynamics Conference and Exhibit, New Orleans, LA, p. 2686 (2012). https://doi.org/10.2514/6.2012-2686
- [31] Amsallem, D., Zahr, M.J., Farhat, C.: Nonlinear model order reduction based on local reduced-order bases. International Journal for Numerical Methods in Engineering 92(10), 891–916 (2012) https://doi.org/10.1002/nme.4371
- [32] Parish, E.J., Carlberg, K.T.: Windowed least-squares model reduction for dynamical systems. Journal of Computational Physics 426, 109939 (2021) https://doi.org/10.1016/j.jcp.2020.109939
- [33] Shimizu, Y.S., Parish, E.J.: Windowed space-time least-squares petrov-galerkin model order reduction for nonlinear dynamical systems. Computer Methods in Applied Mechanics and Engineering 386, 114050 (2021) https://doi.org/10.1016/ j.cma.2021.114050
- [34] Schmid, P.J.: Dynamic mode decomposition of numerical and experimental data. Journal of fluid mechanics **656**, 5–28 (2010) https://doi.org/10.1017/S0022112010001217
- [35] Rowley, C.W., Mezić, I., Bagheri, S., Schlatter, P., Henningson, D.S.: Spectral analysis of nonlinear flows. Journal of fluid mechanics **641**, 115–127 (2009) https://doi.org/10.1017/S0022112009992059
- [36] Tu, J.H., Rowley, C.W., Luchtenburg, D.M., Brunton, S.L., Kutz, J.N.: On dynamic mode decomposition: Theory and applications. Journal of Computational Dynamics 1(2), 391–421 (2014) https://doi.org/10.3934/jcd.2014.1.391
- [37] Proctor, J.L., Brunton, S.L., Kutz, J.N.: Dynamic mode decomposition with control. SIAM Journal on Applied Dynamical Systems **15**(1), 142–161 (2016) https://doi.org/10.1137/15M1013857
- [38] Peherstorfer, B., Willcox, K.: Data-driven operator inference for nonintrusive projection-based model reduction. Computer Methods in Applied Mechanics and Engineering 306, 196–215 (2016) https://doi.org/10.1016/j.cma.2016.03.025
- [39] McQuarrie, S.A., Huang, C., Willcox, K.E.: Data-driven reduced-order models via

- regularised operator inference for a single-injector combustion process. Journal of the Royal Society of New Zealand 51(2), 194-211 (2021) https://doi.org/10. 1080/03036758.2020.1863237
- [40] McQuarrie, S.A., Khodabakhshi, P., Willcox, K.E.: Nonintrusive reduced-order models for parametric partial differential equations via data-driven operator inference. SIAM Journal on Scientific Computing 45(4), 1917–1946 (2023) https: //doi.org/10.1137/21M1452810
- [41] Brunton, S.L., Proctor, J.L., Kutz, J.N.: Discovering governing equations from data by sparse identification of nonlinear dynamical systems. Proceedings of the national academy of sciences 113(15), 3932–3937 (2016) https://doi.org/10.1073/pnas.1517384113
- [42] Messenger, D.A., Bortz, D.M.: Weak sindy: Galerkin-based data-driven model selection. Multiscale Modeling & Simulation 19(3), 1474–1497 (2021) https://doi.org/10.1137/20M1343166
- [43] Fries, W.D., He, X., Choi, Y.: LaSDI: Parametric latent space dynamics identification. Computer Methods in Applied Mechanics and Engineering 399, 115436 (2022) https://doi.org/10.1016/j.cma.2022.115436
- [44] He, X., Choi, Y., Fries, W.D., Belof, J.L., Chen, J.-S.: Glasdi: Parametric physics-informed greedy latent space dynamics identification. Journal of Computational Physics, 112267 (2023) https://doi.org/10.1016/j.jcp.2023.112267
- [45] Kim, B., Azevedo, V.C., Thuerey, N., Kim, T., Gross, M., Solenthaler, B.: Deep fluids: A generative network for parameterized fluid simulations. In: Computer Graphics Forum. Proceedings of Eurographics 2019, vol. 38. Genoa, pp. 59–70 (2019). https://doi.org/10.1111/cgf.13619
- [46] Li, Z., Kovachki, N., Azizzadenesheli, K., Liu, B., Bhattacharya, K., Stuart, A., Anandkumar, A.: Fourier neural operator for parametric partial differential equations. arXiv preprint arXiv:2010.08895 (2020) https://doi.org/10.48550/arXiv.2010.08895
- [47] Kovachki, N., Li, Z., Liu, B., Azizzadenesheli, K., Bhattacharya, K., Stuart, A., Anandkumar, A.: Neural operator: Learning maps between function spaces with applications to PDEs. Journal of Machine Learning Research **24**(89), 1–97 (2023) https://doi.org/10.48550/arXiv.2108.08481
- [48] Lu, L., Jin, P., Pang, G., Zhang, Z., Karniadakis, G.E.: Learning nonlinear operators via deeponet based on the universal approximation theorem of operators. Nature machine intelligence 3(3), 218–229 (2021) https://doi.org/10.1038/ s42256-021-00302-5
- [49] Wang, Y., Cheung, S.W., Chung, E.T., Efendiev, Y., Wang, M.: Deep multiscale

- model learning. Journal of Computational Physics **406**, 109071 (2020) https://doi.org/10.1016/j.jcp.2019.109071
- [50] Cheung, S.W., Chung, E.T., Efendiev, Y., Gildin, E., Wang, Y., Zhang, J.: Deep global model reduction learning in porous media flow simulation. Computational Geosciences 24, 261–274 (2020) https://doi.org/10.1007/s10596-019-09918-4
- [51] Zhang, J., Cheung, S.W., Efendiev, Y., Gildin, E., Chung, E.T.: Deep model reduction-model learning for reservoir simulation. In: SPE Reservoir Simulation Conference, Galveston, TX (2019). https://doi.org/10.2118/193912-MS
- [52] Wang, Y., Lin, G.: Efficient deep learning techniques for multiphase flow simulation in heterogeneous porousc media. Journal of Computational Physics 401, 108968 (2020) https://doi.org/10.1016/j.jcp.2019.108968
- [53] Chen, Z., Xiu, D.: On generalized residual network for deep learning of unknown dynamical systems. Journal of Computational Physics 438, 110362 (2021) https://doi.org/10.1016/j.jcp.2021.110362
- [54] Wan, Z.Y., Vlachas, P., Koumoutsakos, P., Sapsis, T.: Data-assisted reducedorder modeling of extreme events in complex dynamical systems. PloS one 13(5), 0197704 (2018) https://doi.org/10.1371/journal.pone.0197704
- [55] Nguyen, P.C.H., Nguyen, Y.-T., Seshadri, P.K., Choi, J.B., Udaykumar, H., Baek, S.: A physics-aware deep learning model for energy localization in multiscale shock-to-detonation simulations of heterogeneous energetic materials. Propellants, Explosives, Pyrotechnics 48(4), 202200268 (2023) https://doi.org/10.1002/prep.202200268
- [56] Cheng, X., Zhang, S., Nguyen, P.C.H., Azarfar, S., Chern, G.-W., Baek, S.S.: Convolutional neural networks for large-scale dynamical modeling of itinerant magnets. Phys. Rev. Res. 5, 033188 (2023) https://doi.org/10.1103/PhysRevResearch.5.033188
- [57] Li, C., Verduzco, J.C., Lee, B.H., Appleton, R.J., Strachan, A.: Mapping microstructure to shock-induced temperature fields using deep learning. npj Computational Materials 9, 178 (2023) https://doi.org/10.1038/s41524-023-01134-0
- [58] Springer, H.K., Miller, C.M., Kroonblawd, M.P., Bastea, S.: Simulating the effects of grain surface morphology on hot spots in HMX with surrogate model development. Propellants, Explosives, Pyrotechnics 48(4), 202200139 (2023) https: //doi.org/10.1002/prep.202200139
- [59] Amsallem, D., Farhat, C.: Interpolation method for adapting reduced-order models and application to aeroelasticity. AIAA journal **46**(7), 1803–1813 (2008) https://doi.org/10.2514/1.35374

- [60] Amsallem, D., Farhat, C.: An online method for interpolating linear parametric reduced-order models. SIAM Journal on Scientific Computing **33**(5), 2169–2198 (2011) https://doi.org/10.1137/100813051
- [61] Choi, Y., Boncoraglio, G., Anderson, S., Amsallem, D., Farhat, C.: Gradient-based constrained optimization using a database of linear reduced-order models. Journal of Computational Physics 423, 109787 (2020) https://doi.org/10.1016/j.jcp.2020.109787
- [62] Kadeethum, T., O'Malley, D., Choi, Y., Viswanathan, H.S., Bouklas, N., Yoon, H.: Continuous conditional generative adversarial networks for data-driven solutions of poroelasticity with heterogeneous material properties. Computers & Geosciences 167, 105212 (2022) https://doi.org/10.1016/j.cageo.2022.105212
- [63] Pereverzev, A., Sewell, T.: Elastic coefficients of  $\beta$ -HMX as functions of pressure and temperature from molecular dynamics. Crystals **10**(12), 1123 (2020) https://doi.org/10.3390/cryst10121123
- [64] Steinberg, D., Cochran, S., Guinan, M.: A constitutive model for metals applicable at high-strain rate. Journal of applied physics 51(3), 1498–1504 (1980) https: //doi.org/10.1063/1.327799
- [65] Johnson, G.R., Cook, W.H.: A constitutive model and data for metals subject to large strains, high strain rate and high temperatures. In: Proceedings of the 7th International Symposium on Ballistics, vol. 21. The Hague, pp. 541–547 (1983). https://ia800102.us.archive.org/9/items/AConstitutiveModelAndDataForMetals/A%20constitutive%20model%20and%20data%20for%20metals\_text.pdf
- [66] Gray III, G., Idar, D., Blumenthal, W., Cady, C., Peterson, P.: High-and low-strain rate compression properties of several energetic material composites as a function of strain rate and temperature. Technical report, Los Alamos National Lab.(LANL), Los Alamos, NM (United States) (1998). https://www.osti.gov/biblio/329541
- [67] Millett, J., Taylor, P., Roberts, A., Appleby-Thomas, G.: The strength of two HMX based plastic bonded explosives during one dimensional shock loading. Journal of Dynamic Behavior of Materials 3, 100–109 (2017) https://doi.org/10.1007/ s40870-017-0099-1
- [68] Dick, J., Hooks, D., Menikoff, R., Martinez, A.: Elastic-plastic wave profiles in cyclotetramethylene tetranitramine crystals. Journal of Applied Physics 96(1), 374–379 (2004) https://doi.org/10.1063/1.1757026
- [69] Springer, H.K., Bastea, S., Nichols III, A.L., Tarver, C.M., Reaugh, J.E.: Modeling the effects of shock pressure and pore morphology on hot spot mechanisms in HMX. Propellants, Explosives, Pyrotechnics 43(8), 805–817 (2018) https:

### //doi.org/10.1002/prep.201800082

- [70] Simon, F., Glatzel, G.: Bemerkungen zur schmelzdruckkurve. Zeitschrift für anorganische und allgemeine Chemie  $\bf 178(1)$ , 309–316 (1929) https://doi.org/10.1002/zaac.19291780123
- [71] Kroonblawd, M.P., Austin, R.A.: Sensitivity of pore collapse heating to the melting temperature and shear viscosity of HMX. Mechanics of Materials 152, 103644 (2021) https://doi.org/10.1016/j.mechmat.2020.103644
- [72] Fried, L.E., Howard, W.M.: Explicit gibbs free energy equation of state applied to the carbon phase diagram. Physical Review B **61**(13), 8734 (2000) https://doi.org/10.1103/PhysRevB.61.8734
- [73] Marsh, S.P.: LASL Shock Hugoniot Data vol. 5. University of California Press, Berkeley and Los Angeles, USA (1980)
- [74] Olinger, B., Roof, B., Cady, H.: The linear and volume compression of  $\beta$ -HMX and RDX. In: Actes du Symposium International sur Le Comportement des Milieux Denses Sous Hautes Pressions Dynamiques, Paris, pp. 3–8 (1978)
- [75] Yoo, C.-S., Cynn, H.: Equation of state, phase transition, decomposition of β-hmx (octahydro-1, 3, 5, 7-tetranitro-1, 3, 5, 7-tetrazocine) at high pressures. The Journal of Chemical Physics 111(22), 10229–10235 (1999) https://doi.org/10.1063/1.480341
- [76] Gump, J.C., Peiris, S.M.: Isothermal equations of state of beta octahydro-1, 3, 5, 7-tetranitro-1, 3, 5, 7-tetrazocine at high temperatures. Journal of Applied Physics **97**(5) (2005) https://doi.org/10.1063/1.1856227
- [77] Menikoff, R., Sewell, T.D.: Constituent properties of HMX needed for mesoscale simulations. Combustion theory and modelling **6**(1), 103 (2002) https://doi.org/10.1088/1364-7830/6/1/306
- [78] Baytos, J.F.: Specific heat and thermal conductivity of explosives, mixtures, and plastic-bonded explosives determined experimentally. Technical report, Los Alamos National Lab.(LANL), Los Alamos, NM (United States) (1979). https://doi.org/10.2172/5913065
- [79] Goodfellow, I., Pouget-Abadie, J., Mirza, M., Xu, B., Warde-Farley, D., Ozair, S., Courville, A., Bengio, Y.: Generative adversarial nets. In: Ghahramani, Z., Welling, M., Cortes, C., Lawrence, N., Weinberger, K.Q. (eds.) Advances in Neural Information Processing Systems, vol. 27. Montréal (2014). https://proceedings.neurips.cc/paper\_files/paper/2014/file/5ca3e9b122f61f8f06494c97b1afccf3-Paper.pdf

- [80] Radford, A., Metz, L., Chintala, S.: Unsupervised representation learning with deep convolutional generative adversarial networks. arXiv preprint arXiv:1511.06434 (2015) https://doi.org/10.48550/arXiv.1511.06434
- [81] Dupont, E., Zhang, T., Tilke, P., Liang, L., Bailey, W.: Generating realistic geology conditioned on physical measurements with generative adversarial networks. arXiv preprint arXiv:1802.03065 (2018) https://doi.org/10.48550/arXiv. 1802.03065
- [82] Cheung, S.W., Kushwaha, A., Sun, H., Wu, X.-H.: Stochastic representation and conditioning of process-based geological model by deep generative and recognition networks. Petroleum Geoscience, 2022–032 (2024) https://doi.org/10.1144/ petgeo2022-032
- [83] Laloy, E., Hérault, R., Jacques, D., Linde, N.: Training-image based geostatistical inversion using a spatial generative adversarial neural network. Water Resources Research 54(1), 381–406 (2018) https://doi.org/10.1002/2017WR022148
- [84] Demir, U., Unal, G.: Patch-based image inpainting with generative adversarial networks. arXiv preprint arXiv:1803.07422 (2018) https://doi.org/10.48550/arXiv.1803.07422
- [85] Ronneberger, O., Fischer, P., Brox, T.: U-net: Convolutional networks for biomedical image segmentation. In: Medical Image Computing and Computer-Assisted Intervention—MICCAI 2015, Munich, pp. 234–241 (2015). https://doi.org/10.1007/978-3-319-24574-4\_28
- [86] Isola, P., Zhu, J.-Y., Zhou, T., Efros, A.A.: Image-to-image translation with conditional adversarial networks. In: Proceedings of the IEEE Conference on Computer Vision and Pattern Recognition, Honolulu, HI, pp. 1125–1134 (2017). https://openaccess.thecvf.com/content\_cvpr\_2017/html/Isola\_ Image-To-Image\_Translation\_With\_CVPR\_2017\_paper.html
- [87] Arjovsky, M., Chintala, S., Bottou, L.: Wasserstein generative adversarial networks. In: Precup, D., Teh, Y.W. (eds.) Proceedings of the 34th International Conference on Machine Learning. Proceedings of Machine Learning Research, vol. 70, pp. 214–223. PMLR, Sydney (2017). https://proceedings.mlr.press/v70/arjovsky17a.html
- [88] Ding, X., Wang, Y., Xu, Z., Welch, W.J., Wang, Z.J.: Continuous conditional generative adversarial networks: Novel empirical losses and label input mechanisms. IEEE Transactions on Pattern Analysis and Machine Intelligence 45(7), 1–16 (2022) https://doi.org/10.1109/TPAMI.2022.3228915
- [89] Gulrajani, I., Ahmed, F., Arjovsky, M., Dumoulin, V., Courville, A.C.: Improved training of Wasserstein GANs. In: Guyon, I., Luxburg, U.V., Bengio, S., Wallach, H., Fergus, R., Vishwanathan, S., Garnett, R.

- (eds.) Advances in Neural Information Processing Systems, vol. 30. Long Beach, CA (2017).  $https://proceedings.neurips.cc/paper_files/paper/2017/file/892c3b1c6dccd52936e27cbd0ff683d6-Paper.pdf$
- [90] Kingma, D.P., Ba, J.: Adam: A method for stochastic optimization. arXiv preprint arXiv:1412.6980 (2014) https://doi.org/10.48550/arXiv.1412.6980